High resolution modeling of dense water formation in the north-western Mediterranean during winter 2012-2013: Processes and budget

Claude Estournel, Pierre Testor, Pierre Damien, Fabrizio d'Ortenzio, Patrick Marsaleix, Pascal Conan, Faycal Kessouri, Xavier Durrieu de Madron, Laurent Coppola, Jean-Michel Lellouche, et al.

AGU PUBLICATIONS

JGR

Journal of Geophysical Research: Oceans

RESEARCH ARTICLE
10.1002/2016JC011935

Special Section:
Dense Water Formations in the North Western Mediterranean: From the Physical Forcings to the Biogeochemical Consequences

High resolution modeling of dense water formation in the north-western Mediterranean during winter 2012–2013: Processes and budget

Claude Estournel[1], Pierre Testor[2], Pierre Damien[1], Fabrizio D'Ortenzio[3], Patrick Marsaleix[1], Pascal Conan[4], Faycal Kessouri[1], Xavier Durrieu de Madron[5], Laurent Coppola[3], Jean-Michel Lellouche[6], Sophie Belamari[7], Laurent Mortier[2,8], Caroline Ulses[1], Marie-Noelle Bouin[9], and Louis Prieur[3]

[1]Université de Toulouse, CNRS, UPS, Laboratoire d'Aérologie, Toulouse, France, [2]Sorbonne Universités, UPMC Univ Paris 06, CNRS, IRD, MNHN, LOCEAN, Paris, France, [3]Sorbonne Universités, UPMC Univ Paris 06, CNRS, LOV, Villefranche sur Mer, France, [4]Sorbonne Universités, UPMC Univ Paris 06, CNRS, Laboratoire d'Océanographie Microbienne, Banyuls sur Mer, France, [5]Université de Perpignan Via Domitia, CNRS, CEFREM, Perpignan, France, [6]Mercator-Océan, Ramonville Saint Agne, France, [7]CNRM-GAME, UMR3589, Météo-France – CNRS, Toulouse, France, [8]UME ENSTA, Palaiseau, France, [9]CMM, Météo-France, Brest, France

Key Points:
- Realistic simulation of winter convection and dense water formation
- Correction of initial and boundary conditions improves the simulation
- Sensitivity studies to air - sea fluxes are characterized

Correspondence to:
C. Estournel,
claude.estournel@aero.obs-mip.fr

Citation:
Estournel, C., et al. (2016), High resolution modeling of dense water formation in the north-western Mediterranean during winter 2012–2013: Processes and budget, *J. Geophys. Res. Oceans*, *121*, 5367–5392, doi:10.1002/2016JC011935.

Received 4 MAY 2016
Accepted 30 JUN 2016
Accepted article online 4 JUL 2016
Published online 31 JUL 2016

Abstract The evolution of the stratification of the north-western Mediterranean between summer 2012 and the end of winter 2013 was simulated and compared with different sets of observations. A summer cruise and profiler observations were used to improve the initial conditions of the simulation. This improvement was crucial to simulate winter convection. Variations of some parameters involved in air - sea exchanges (wind, coefficient of transfer used in the latent heat flux formulation, and constant additive heat flux) showed that the characteristics of water masses and the volume of dense water formed during convection cannot be simply related to the time-integrated buoyancy budget over the autumn - winter period. The volume of dense water formed in winter was estimated to be about 50,000 km^3 with a density anomaly larger than 29.113 kg m^{-3}. The effect of advection and air/sea fluxes on the heat and salt budget of the convection zone was quantified during the preconditioning phase and the mixing period. Destratification of the surface layer in autumn occurs through an interaction of surface and Ekman buoyancy fluxes associated with displacements of the North Balearic front bounding the convection zone to the south. During winter convection, advection stratifies the convection zone: from December to March, the absolute value of advection represents 58 % of the effect of surface buoyancy fluxes.

1. Introduction

The Mediterranean Sea is like the Greenland, the Labrador and the Weddell seas, a region of deep winter convection and deep water formation [*Marshall and Schott*, 1999]. The very typical climatic characteristics of the basin, with mainly cold and dry local winds blowing from the north and inducing high evaporation, produce open sea convection in the Aegean [*Nittis et al*., 2003], Adriatic *[Manca et al*., 2002] and north-western Mediterranean [*Schott et al*., 1996]. Deep convection in the north-western Mediterranean is the main mechanism of deep water renewal in the western Mediterranean basin. Cascading of dense water formed on the continental shelves is also an important mechanism for the ventilation of intermediate and deep waters in the oceans [*Ivanov et al*., 2004]. In the north-western Mediterranean Sea, it forms more occasionally water dense enough to cascade downslope to the deep basin ($>$ 2000 m) [*Puig et al*., 2013]. Various studies have helped to clarify the interannual variability of convection [*Mertens and Schott*, 1998; *Béthoux et al*., 2002]. To a first approximation, the link between convection variability and climate variability is clear: when winters are especially cold, convection is deep and can reach the sea floor ($>$ 2500 m). This was the case for the winters 1986-1987 [*Leaman and Schott*, 1991; *Herrmann et al*., 2008a] and 2004-2005 [*López-Jurado et al*., 2005; *Herrmann et al*., 2010], for example. Conversely, the repeated absence of cold winters, as in the 1990s, inhibited convection. This resulted in the accumulation of salt and heat in the intermediate waters which altered the stratification before the winter of 2004-2005.

In recent years, increasing numbers of observations have enabled the hydrological characteristics of newly-formed dense water to be monitored. Several authors have highlighted changes in these characteristics since the winter of 2005 [*López-Jurado et al*., 2005; *Schröder et al*., 2006; *Puig et al*., 2013; *Schroeder et al*., 2016]. However, it is much more difficult to assess the volume of this newly-formed dense water even though indirect estimates based on a combination of information have become available for recent periods. For example, *Durrieu de Madron et al*. [2013] proposed an estimation of the volume of dense water formed during winter 2011-2012 based on a completely mixed vertical density profile and a satellite image of chlorophyll. This information on volume is important, for example to determine the amount of dissolved oxygen that ventilates the deeper layers.

Because of the importance of deep convection on the thermohaline circulation and the marine ecosystems, and in the context of climate change, the monitoring of annual convection and of the characteristics of deep water is a priority of MOOSE, the French observation system for the north-western Mediterranean (http://www.moose-network.fr). Since 2007, a mooring line completed close to the surface by a thermistor string fixed under a nearby meteorological buoy, has enabled high frequency monitoring of the stratification near the center of the convection zone (42° N, 4°40 E). To complete this 1D vertical description of stratification, it was decided to take advantage of the mooring maintenance cruise to carry out a conductivity-temperature-depth (CTD) survey at the scale of the north-western basin. The MOOSE-GE cruise has been organized in summer every year since 2010. It has achieved an average of ∼70 CTD surface to bottom profiles to highlight the characteristics of deep water possibly formed in the previous winter [*Durrieu de Madron et al*., 2013]. However, the volume of newly-formed dense water remains difficult to evaluate from these observations because of the dilution that occurs during the few intervening months and the spread of this water beyond the area that can be explored in the context of the cruise. **The first objective** of this paper is thus to associate high resolution modeling with the observation network to determine the volume of water formed during winter. To the best of our knowledge, it is the first time that this experiment has been carried out as, until recent years, no synoptic data set was available in a region of dense water formation. The realism of the modeling was thus limited, for example to 1-D cases, to simulate the evolution of the mixed layer starting from an observation of temperature and salinity profiles (see results in the Labrador and Mediterranean seas presented in *Marshall and Schott* [1999] or *Sproson et al*. [2008] in the Labrador Sea).

In our case, a numerical model was implemented at high resolution at the scale of the north- western Mediterranean with an accurate initial state based on the MOOSE-GE cruise. To test its ability to represent convection 6 months after the model initialization, we chose to simulate the year 2012-2013 because, in addition to the MOOSE-GE-2012 cruise in summer 2012, other cruises with similar sampling patterns but at different times of the year, between September 2012 and April 2013, were available. The cruise of February 2013 during convection allowed the efficiency of the method to be checked.

Dense water formation is usually studied in a conceptual framework based on the succession of 3 periods: preconditioning at the scale of the cyclonic gyre, convection dominated by vertical mixing processes at the scale of the mixed patch and restratification/spreading dominated by baroclinic instabilities developing at the periphery of the mixed patch [*Marshall and Schott*, 1999]. However, *Jones and Marshall* [1997] pointed out that field observations clearly showed that vigorous geostrophic eddy activity occurred not only after but also during violent convective mixing. In contrast, *L'Hévéder et al*. [2013], basing their work on a long simulation with an eddy-permitting model, found that deep convection was likely to occur when the surface buoyancy fluxes integrated from 1st December exceeded the buoyancy flux required to mix the initial water column down to the convective threshold depth of 1200 m. This means that, as a first approximation, deep convection would reduce to a 1D process. This result should be tempered as mesoscale structures are not correctly represented in eddy-permitting ocean models and so advection they could induce in the convection site would be underestimated [*Herrmann et al*., 2008a]. Moreover, the initial date, chosen in December in *L'Hévéder et al*. [2013] restrained the analysis to the winter months once the strong stratification of the first tens of meters had been eroded.

In this context, where various time scales and processes appear to be imbricated, **our second objective** is to use our high resolution simulation to study the processes that contribute to the destruction of the stratification during the preconditioning period (autumn) and during the convective period (winter) and to establish a heat and salt budget for the convection zone. In more detail, the following questions are addressed: What is the efficiency of 1D processes to erase the stratification and does advection play an important role?

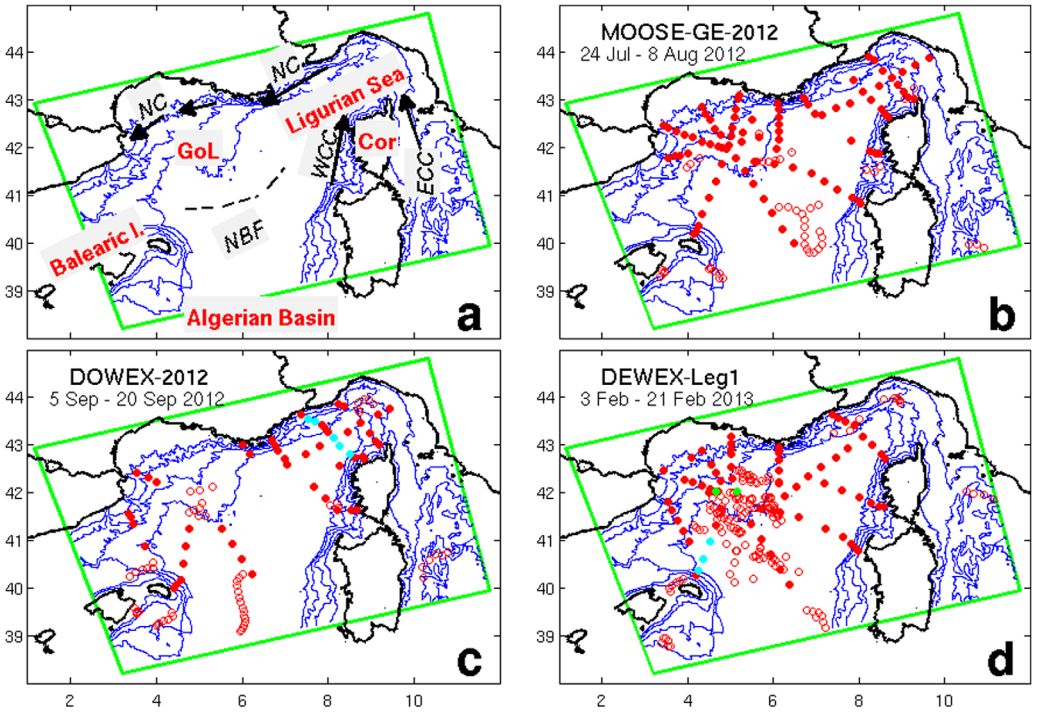

Figure 1. (a) Map of the north-western Mediterranean with the geographical indications cited in the text written in red (GoL for Gulf of Lion, Cor for Corsica) and oceanic features in black (WCC for Western Corsica Current, ECC for Eastern Corsica Current, NC for Northern Current and NBF for North Balearic Front); (b–d) Position of temperature and salinity profiles used during the three periods documented between summer 2012 and winter 2012–2013 as indicated by the name of the cruise. Filled circles: position of CTD profiles measured during cruises, open circles: position of the Argo profiles. Blue circles on the DOWEX-2012 cruise map correspond to profiles plotted on Figure 3. Green circles on the DEWEX-Leg1 cruise map correspond to profiles 52 and 53 and blue circles to profiles 25, 26 and 27 discussed in sections 3.2.2 and 3.2.3 respectively. The green rectangle indicates the limits of the area of the model. Blue lines are the 200, 1000, 2000 and 2500 m isobaths of the model.

Is there a difference between the relative importance of these 1D and 3D processes in autumn, when the mixed layer is shallow ($<$ 100 m), and in winter? Most studies on this topic have been devoted to the winter period because it is the period of the "fascinating and central aspect of the convective process in the ocean, that is the interaction between convection and baroclinic instability" [*Marshall and Schott*, 1999].

The second section of this paper presents the observations and the numerical model used in the study, then the method used to correct the initial state of the model and its lateral boundary conditions. Section 3 presents the sensitivity of the representation of convection by the model to its initial state and to the uncertainties on atmospheric forcing. Section 4 presents the evolution of the stratification in the convection zone from summer to winter based on a carefully validated simulation. Section 5 gives details of the heat and salt budget during the preconditioning and the convective periods. Section 6 discusses the importance of the realism of the initial state and of the high horizontal resolution in representing the time evolution of stratification in autumn and winter. Section 7 concludes the paper.

2. Material and Methods

2.1. Observations

A large set of observations (High quality CTD Seabird SBE9 profiles) collected during three cruises were available for July-August 2012 (MOOSE-GE-2012 cruise, MOOSE program, [*Testor et al*., 2012]), September 2012 (DOWEX-2012 cruise, MerMex program), and February 2013 (DEWEX-Leg1 cruise, MerMex program, [*Testor*, 2013]) in the north-western Mediterranean. They used a common network but did not have the same numbers of stations (Figures 1b–1d) due to unforeseeable sampling complications (i.e., unfavorable sea state and access restriction to some areas by naval authorities). The network covered the Gulf of Lion and the Ligurian Sea, areas where deep mixing and deep water formation occur regularly. Observations spread throughout the area are organized along sections perpendicular to the general circulation (Northern

Table 1. Description of Observations Used During the Three Periods Discussed in This Paper

Cruise	Period	Number of CTD	Period Considered for Argo	Number of Argo Profiles
MOOSE-GE-2012	24 Jul. to 8 Aug. 2012	88	15 Jul. to 15 Aug. 2012	52
DOWEX-2012	5 Sep. to 20 Sep. 2012	54	28 Aug. to 27 Sep. 2012	60
DEWEX-Leg1	3 Feb. to 21 Feb. 2013	75	28 Jan. to 26 Feb. 2013	139

Current, recirculation associated with the Balearic front and West Corsica Current – see Figure 1a). During the same periods, Argo profiles were also available for the region, their number being significantly increased during winter thanks to the HyMeX program, which deployed three floats producing daily profiles in the central area of the Gulf of Lion from 28 January 2013. Three sets of data were compiled by associating one month of Argo profiles with each CTD cruise. Each month of Argo data was centered on the median day of the cruise (Figure 1). Table 1 summarizes the observations used for the three periods. Finally, this study used the data of the meteorological buoy named LION anchored in the convection zone at 42.06°N, 4.64°E equipped with temperature sensors every 5-10 m in the first 100 m and every 20-25 m from 100 to 200 m under the sea surface.

2.2. Numerical Modeling

This study used the free surface, generalized sigma vertical coordinate, 3D model SYMPHONIE described by *Marsaleix et al*. [2008, 2009, 2012]. This model has previously been used in the Mediterranean to simulate convection in the open sea [*Herrmann et al*., 2008a], as well as coastal dense water formation [*Ulses et al*., 2008; *Estournel et al*., 2005; *Herrmann et al*., 2008b]. The vertical diffusion is parameterized following *Gaspar et al*. [1990] with a prognostic equation for the turbulent kinetic energy and a diagnostic equation for the mixing and dissipation lengths. The size of the grid is not small enough to explicitly represent convective plumes, which thus need to be parameterized. Without parameterization of convection, the buoyancy loss at the surface produces static instability resulting in noise at the scale of the mesh (alternating positive and negative vertical velocities). Different parameterizations have been proposed to overcome this problem [e.g., *Marsland et al*., 2003]. In our case, the heat and water fluxes are distributed over the whole mixed layer. Its depth is given by the depth at which the vertical density gradient becomes negative. Thus the first level under the surface does not support the entire amount of heat loss by itself, which prevents the development of static instabilities at the surface. Furthermore, this parameterization is consistent with the nearly linear variation in z of the buoyancy flux in the convective layer [*Deardorff et al*., 1969].

The model domain is shown in Figure 1 (green frame). It covers the entire convection zone with a horizontal resolution of 1 km (to our knowledge, higher than in any other realistic studies of convection in the northwestern Mediterranean) to represent the scales related to the Rossby radius, of the order of 5-10 km. Forty vertical levels were used with closer spacing near the surface (15 levels in the first 100 meters in the center of the convection zone characterized by water depths of ∼2500 m).

A first guess for initial and boundary conditions was prescribed from bilinearly interpolated daily-averaged fields provided by Mercator-Océan. These fields come from the regional analysis and forecasting operational system PSY2V4R2 covering the Atlantic and the Mediterranean between 20° S and 80° N with a 1/12° horizontal grid spacing (∼7 km over the Mediterranean) and 50 vertical levels. This system is based on the NEMO (Nucleus for European Modeling of the Ocean) ocean-modeling platform and on the SAM (*Système d'Assimilation Mercator*) data assimilation system [*Lellouche et al*., 2013]. Altimeter data, satellite sea surface temperature and in situ temperature and salinity vertical profiles are assimilated by means of a reduced-order Kalman filter with a 3-D multivariate modal decomposition of the forecast error.

The atmospheric forcing of the high resolution model was calculated using the bulk formulae of *Large and Yeager* [2004]. Section 3 analyzes the sensitivity of the convection to the air/sea fluxes. To better understand how this sensitivity was explored, the expression for air/sea fluxes is given below. The wind stress module τ expressed in N/m^2 is a quadratic function of the wind U:

$$\tau = \rho_a C_D U^2 \quad (1)$$

where ρ_a is the air density and C_D is the drag coefficient.

The surface heat budget in W/m^2 is given by:

$$Q_{net}=Q_S+Q_L+Q_H+Q_E \tag{2}$$

where downward fluxes are defined positive. Q_S and Q_L are the shortwave and longwave net radiative fluxes both of them being the sum of downward and upward components. Q_H and Q_E are the turbulent sensible and latent heat fluxes given by:

$$Q_H=\rho_a\, C_{pa}\, C_H\, U\,(\theta-SST)\quad Q_E=\rho_a\, C_E\, U\,(q_a-q_{sat}(SST)) \tag{3}$$

where C_{pa} is the specific heat of the air (J kg^{-1} °C^{-1}), SST is the sea surface temperature, θ and q_a are the air potential temperature and specific humidity, $q_{sat}(SST)$ represents the specific humidity at saturation for air in contact with the sea surface, and C_H and C_E are transfer coefficients for sensible heat and evaporation. The water budget W(m s^{-1}) is given by the difference between precipitation P and evaporation, itself proportional to the latent heat flux with the constant L being the latent heat of vaporization (J kg^{-1}):

$$W=P+\frac{Q_E}{\rho_w L} \tag{4}$$

Meteorological parameters U, T, q_a, P_0 (where T and P_0 are the air temperature and sea level atmospheric pressure, both necessary to calculate θ), the downward shortwave and longwave fluxes and the precipitation came from the ECMWF operational forecasts at 1/8° horizontal resolution and 3 hours temporal resolution. These forecasts were derived from the daily analysis at 00.00 UTC.

The high-resolution simulation discussed here was initialized on 1 August 2012, the median date of the MOOSE-GE-2012 cruise. It finished at the end of April 2013 with the end of the PSY2V4R2 ocean analysis operational system.

2.3. Correction of the Initial State and Boundary Conditions

Despite the data assimilation of the operational system, biases existed on the vertical ocean stratification as will be detailed later. This was due, on the one hand, to the absence of data below 2000 m, and on the other, to the low volume of real-time data on the large model domain (Atlantic Mediterranean). As far as the scale of the north-western Mediterranean is concerned and for the period of the summer cruise, the data set collected allowed to be more precise. To improve the realism of the model initial conditions, 3-D fields of temperature and salinity corrections were calculated from the anomalies of the first guess, relative to the observations.

Anomalies calculated at each observation point of the first cruise were analyzed on the model grid. Two methods were tested: first a purely isotropic analysis (equation (5)) and, second, the weighting of equation (5) by a function accounting for similarities in the hydrological characteristics of the water masses (equation (6)).

$$T^{\text{model}}_{i,j,k\ iso}=T^{fg}_{i,j,k}+\frac{\sum_{obs}(\overline{T^{obs}-T^{fg}_{i_{obs}j_{obs}}})\exp\left(-\frac{d^2}{d_0{}^2}\right)}{\delta+\sum_{obs}\exp\left(-\frac{d^2}{d_0{}^2}\right)} \tag{5}$$

$$T^{\text{model}}_{i,j,k\ aniso}=T^{fg}_{i,j,k}+\frac{\sum_{obs}(\overline{T^{obs}-T^{fg}_{i_{obs}j_{obs}}})\exp\left(-\frac{d^2}{d_0{}^2}\right)\exp\left(-\frac{\left(\rho^{fg}_{i,j,k}-\rho^{fg}_{i_{obs}j_{obs}z(i,j,k)}\right)^2}{\Delta\rho^2_0(z)}\right)}{\delta+\sum_{obs}\exp\left(-\frac{d^2}{d_0{}^2}\right)\exp\left(-\frac{\left(\rho^{fg}_{i,j,k}-\rho^{fg}_{i_{obs}j_{obs}z(i,j,k)}\right)^2}{\Delta\rho^2_0(z)}\right)} \tag{6}$$

These equations are given for temperature but the same form was used for salinity. The indices i, j, k correspond to the model grid, z is the depth at grid point (i,j,k). The second term on the right–hand side of equation (5) is the correction added to the first guess (*fg*). It depends on the difference between the value measured by each CTD and the value of the first guess at the same point, this difference being weighted by a function of the distance between the grid point where the correction is calculated and the observation. δ is a constant taken to be equal to exp (-4) and used to cancel the correction at large distances from all

observations. The average bar indicates that the differences are vertically averaged over the layer (i,j,k). The exponential function characterizing the anisotropy (last term in equation (6)) is used to propagate the correction preferentially in a water mass with similar hydrological characteristics. "Similarities" in salinity and temperature or, alternatively, directly in density (case of equation (6)) were tested. The latter case was chosen as it provided the best results (see criterion below). We chose to calculate the "density characteristic scale" at each vertical level from the density range in the model field:

$$\Delta\rho_0(z)=\frac{(\rho_{\max}(z)-\rho_{\min}(z))}{a} \tag{7}$$

Finally, the procedure used to correct the initial state was also applied to the second and third cruises to renew the corrections at the model's open boundary, which were then time-interpolated.

The choice of the constant a and of the characteristic distance d_0, the ranking of equations (5) and (6) and more generally the analysis of several sensitivity studies presented in the next section were made with a criterion of minimum deviation from the cruises observations. The stratification in the observed density profiles and in the density profiles simulated at the same dates and the same points was characterized by a stratification index F:

$$F(Z)=\int_Z^0(\rho(Z)-\rho(z))\,dz \tag{8}$$

representing the amount of buoyancy in kg m^{-2} to be extracted to mix the water column from the surface to level Z and achieve a homogeneous density $\rho(Z)$. For each observation from a cruise, the vertical profile of the difference $\Delta F=F_{obs}-F_{mod\,el}$ was calculated and then, all the profiles ΔF from the cruise were averaged. A smaller absolute value of ΔF signified closer observed and simulated stratifications.

3. Sensitivity to Initial Stratification and Atmospheric Fluxes

3.1. Efficiency of the Correction of Initial Conditions

The method used to correct the initial state was calibrated with the DOWEX 2012 cruise (median day 42 days after the model initialization). The proximity to the initial state indicated whether the corrections made to the initial state were "digested" by the model as it was possible that such perturbations might produce numerical adjustments (initial spin-up period), through a propagation of gravity waves, that might in turn, destroy part of the initial state improvement.

Figure 2 shows the mean and standard deviation of the stratification index anomaly profile $F_{obs}-F_{\text{model}}$ for all CTD of the September 2012 cruise and for three simulations the characteristics of which are presented in the first part of Table 2. The first is the simulation without correction *No corr* the second and third are the simulations with the initial and boundary conditions corrected by the isotropic interpolation (equation (5) named *Corr iso*) or the anisotropic interpolation (equation (6) named *Corr aniso*) respectively. The constant d_0 involved in (5) and (6) was taken as 100 km. This rather high value was imposed by the star shape of the network and, more particularly, by the distance between the branches located in the southern part of the domain. A sensitivity study showed that a value of 150 km gave results close to those obtained with 100 km, while a value of 50 km did not provide continuity of the interpolated fields for the geometric considerations discussed before. The constant a in equation (7) was set to 12 since lower values gave poorer results (values tested from 2), while higher values led to noisy interpolated fields.

In Figure 2, negative values of the stratification index anomaly at a level z indicate a simulated stratification that is generally too strong in the layers between the surface and z. The simulation *No corr* is the one with the most excessive stratification. The minimum at 1500 m indicates that, above this depth, stratification is overestimated, while inversion of the curve below indicates too weak a stratification in the deeper layers. The other two simulations show a clear improvement in the score. The *Corr iso* simulation corrected with the isotropic interpolation (equation (5)) retains the same profile shape of the stratification index anomaly but its value is reduced by a factor close to 2. The score of the *Corr aniso* simulation corrected with the anisotropic interpolation (equation (6)), which propagates temperature and salinity anomalies preferentially in water masses with similar characteristics, is improved by approximately 30% compared to *Corr iso*. The almost constant value of the stratification index anomaly below 700 meters indicates that, on average,

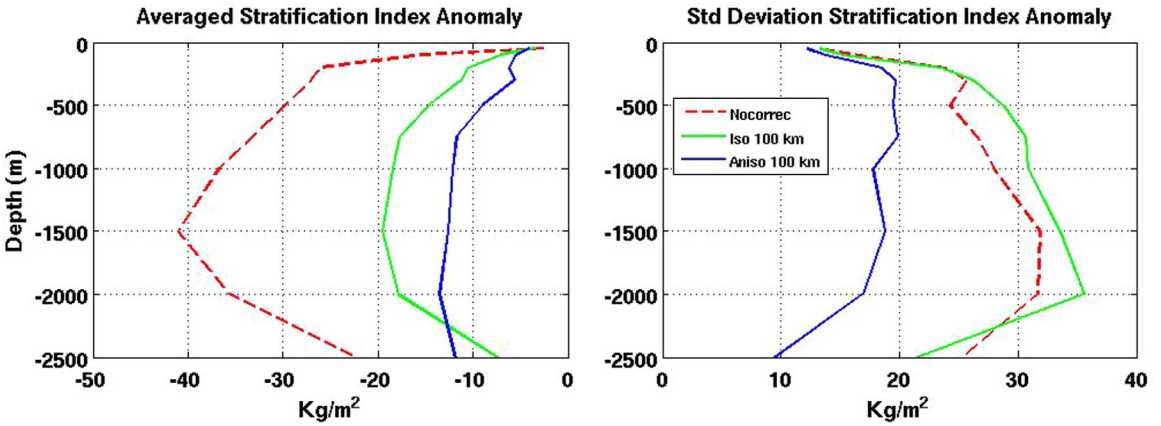

Figure 2. Vertical profiles of the stratification index anomalies for different simulations. (left) anomaly (observation-model) averaged over the available profiles of the DOWEX-2012 cruise in September 2012, (right) standard deviation of the anomaly. Red: simulation without correction, green: isotropic correction with a radius of 100 km (*Corr iso* simulation), blue: anisotropic correction with a radius of 100 km (*Corr aniso* simulation).

stratification is correctly reproduced in this layer (with a slight bias). Finally, this last simulation presents a standard deviation of the stratification index anomaly that is significantly lower and more constant than in the other two simulations (Figure 2, right).

The temperature and salinity profiles observed and calculated by the three simulations are compared in Figure 3 for five CTD stations. The stations were selected on a transect normal to the coast between the Ligurian coast and Corsica (blue circles in Figure 1c). Below 1500 m, observed profiles were almost always better reproduced by both corrected simulations. At intermediate depths (200-1500 m), the *Corr aniso* simulation usually gave the best results. For example, the Levantine Intermediate Water (LIW), with its maximum of

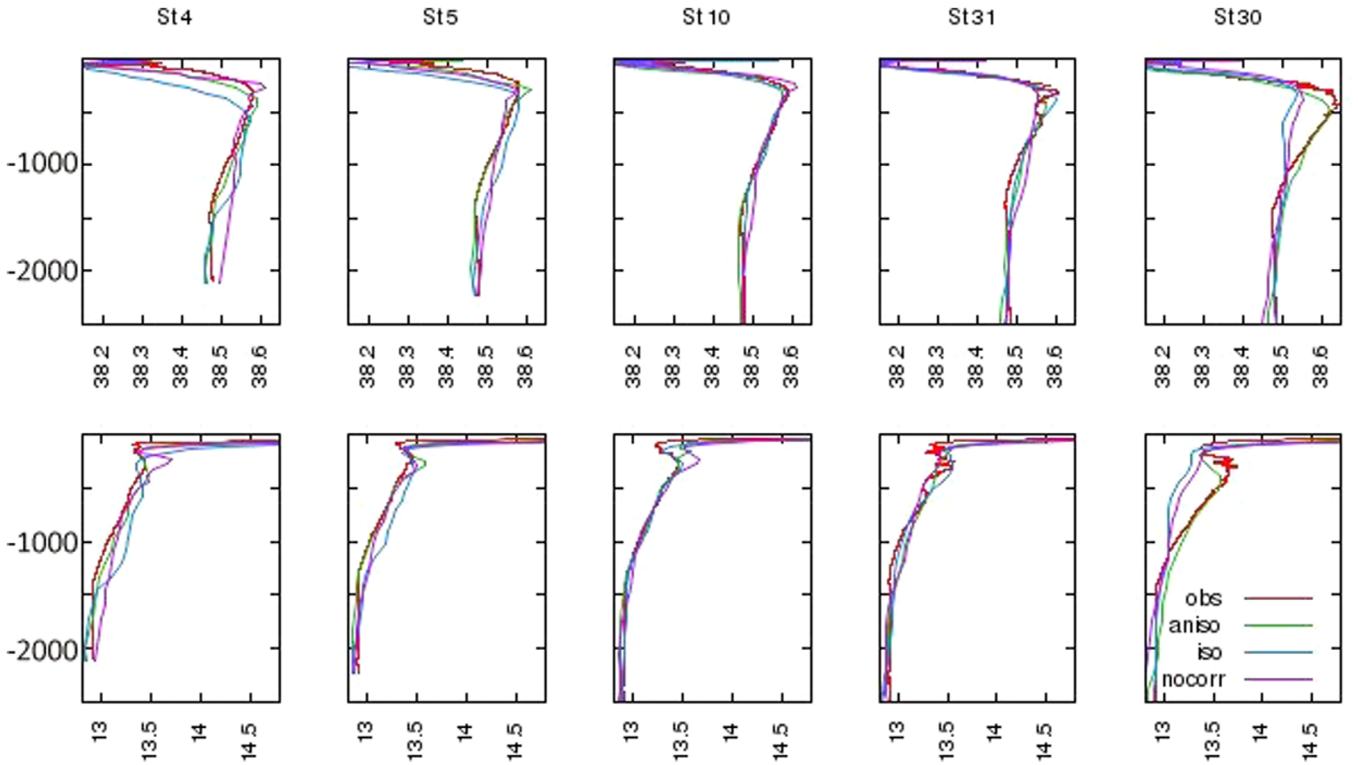

Figure 3. Profiles of (top) salinity and (bottom) potential temperature observed and simulated at different stations of the DOWEX-2012 cruise in September 2012 (see blue circles in Figure 1c). Stations are presented from the north (St 4) to the south (St 30). Red: observation, magenta: *No corr* simulation, cyan: isotropic correction with a radius of 100 km (*Corr iso* simulation), green: anisotropic correction with a radius of 100 km (*Corr aniso* simulation).

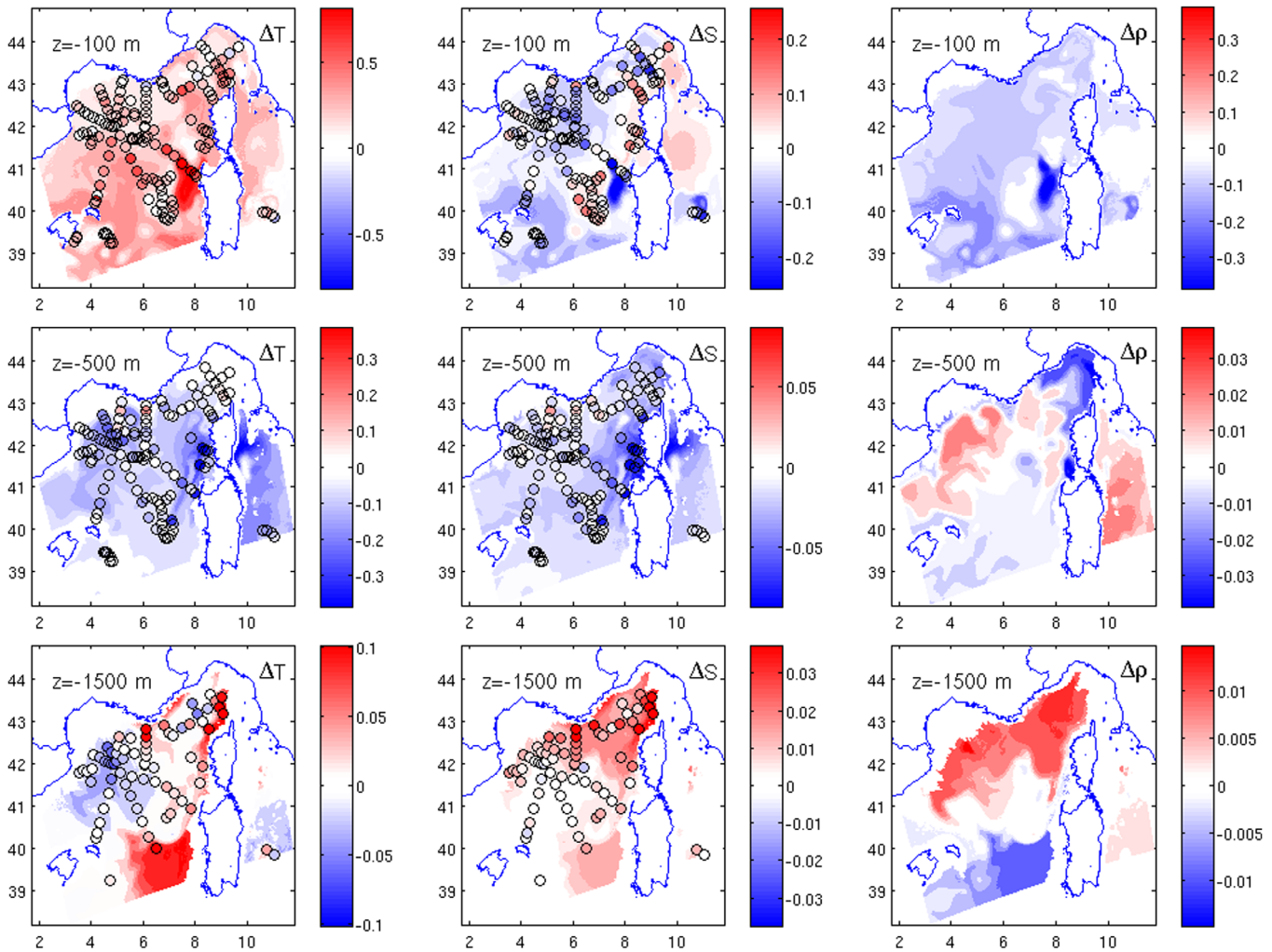

Figure 4. (left) Temperature in °C and (middle) salinity anomalies at three vertical levels. (right) The density anomaly in kg m^{-3} deduced from temperature and salinity anomalies. Circles represent the anomaly (first guess – observation) calculated at the observation points of the MOOSE-GE-2012 cruise in July–August 2012. The colored background map is the interpolation of the anomalies calculated with equation (6) (*Corr aniso*) and used to correct the model first guess ($\Delta T = T_{first\ guess} - T_{initial\ state}$).

salinity and temperature, entering in the north-west Mediterranean along the coast of Corsica (see Station 30) was much better represented over a large range of depths (between 350 m and 1000 m). This feature was not found with *Corr iso*. This result is all the more important as this water mass has been found to have a major impact on the progress of convection [*Grignon et al*., 2010].

Spatial structures of the temperature and salinity anomalies correcting the first guess to give the initial state of *Corr aniso* are shown at three vertical levels in Figure 4 (anomaly=first guess - initial state). Anomalies at the CTD points from which the interpolation was calculated have been superimposed (anomaly=first guess-observation). Additionally, the density anomalies resulting from temperature and salinity anomalies are also represented. The overestimated stratification of the first guess (*No corr*) discussed above is clearly visible in the convection zone in the center of the Gulf of Lion and in the Ligurian Sea, with density anomalies increasing from the surface to 1500 m. These anomalies at depth are generally linked to too low a temperature in the first guess, while temperature and salinity are both responsible for the bias near the surface. Around the areas of convection, along the topographic slope, the density anomaly is related to the salinity of the first guess being too low in the intermediate water. The north-western Mediterranean is characterized by a doming of isopycnals in the Gulf of Lion and the Ligurian Sea [*Marshall and Schott*, 1999] with density gradients generally oriented normal to the topographic slope. Density anomalies noticed here thus impact this hydrological structure. At the initial state, the doming of the *No corr* simulation is too pronounced (density too high in the central part and too low on the slope).

Table 2. Summary of the Simulations Presented in Two Sections of the Paper[a]

Simulation Name	Stratification Correction	Atmospheric Correction
Section 3.1		
No corr	NO	NO
Corr iso	Equation (5)	NO
Corr aniso	Equation (6)	NO
Section 3.2		
No corr	NO	NO
No atm corr	Equation (6)	NO
Vx1.1	Equation (6)	Wind velocity × 1.1
Vx1.13	Equation (6)	Wind velocity × 1.13
Vx1.15	Equation (6)	Wind velocity × 1.5
LHF×1.1	Equation (6)	$C_E \times 1.1$
LHF×1.25	Equation (6)	$C_E \times 1.25$
LHF×1.4	Equation (6)	$C_E \times 1.4$
LWF-11	Equation (6)	$Q_{net} - 11$ W m^{-2}
LWF-15	Equation (6)	$Q_{net} - 15$ W m^{-2}
LWF-20	Equation (6)	$Q_{net} - 20$ W m^{-2}

[a]The first three simulations were used to check the efficiency of the correction of the initial stratification with the September 2012 cruise and the others to test the impact of this correction and of air sea flux corrections on the February 2013 cruise. The shaded line corresponds to the simulation used for the fourth and subsequent sections.

Taken together, these results indicate that a simple interpolation (*Corr iso* equation (5)) can correct the simulation in the case of large-scale errors (case of deep waters). The anisotropic relation (*Corr aniso* equation (6)) can also correct smaller-scale errors associated with the hydrological characteristics of the region. The success of equation (6) indicates that errors are partly organized along isopycnals. The initial state of *Corr aniso* will be used in the rest of this study.

3.2. Sensitivity of Convection to Initial State and Atmospheric Forcing

Concerning atmospheric forcing, we first focused on two well-known sources of uncertainty: (1) the underestimation of strong winds [*Herrmann et al*., 2011] and (2) uncertainties in the parameterizations of turbulent fluxes [*Hauser et al*., 2003]. We also considered a third source of uncertainty, an error independent of wind conditions, which could correspond to an error on the longwave flux Q_L (the term of the heat budget that is the most constant in time). These three sources of error were explored empirically and independently by varying three parameters separately. The first was a constant multiplying the wind, U, as proposed by *Pettenuzzo et al*. [2010] for the correction of the ERA40 reanalysis, the second was also a constant, which directly multiplied the transfer coefficient for evaporation, C_E, involved in the latent heat flux (equation (3)) and calculated following *Large and Yeager* [2004], and the third was a constant added to the surface heat budget, equation (2) (for the sake of simplicity, this correction is named the longwave flux correction hereafter). Unlike the first two errors, which are important mainly during intense events as the turbulent heat fluxes are proportional to the wind and the wind stress is a quadratic function of it, the third affects the whole period. Note also, in the case of the first source of error, that increasing the wind induces a direct modification of the wind stress and of the latent and sensible heat fluxes.

3.2.1. Stratification Index

As in the first part of the paper, the stratification index anomaly relative to observations was used to diagnose and assess the effect of air-sea flux corrections. Anomalies were therefore calculated with respect to the CTD profiles of the DEWEX-Leg1 cruise of February 2013, which took place in a period of significant convection with well mixed stations in the center of the region and others much more stratified at the periphery. Corrections of meteorological parameters or fluxes were applied from the model initialization on 1 August 2012. Stratification corrections to the initial state and to the open boundaries were those obtained with the anisotropic interpolation equation (6). The different characteristics of the simulations used in the following parts (the stratification and atmospheric corrections) are summarized in the second part of Table 2.

Figure 5 presents the mean and the standard deviation of the stratification index anomaly on the 75 CTD stations, for different amplitudes of the corrections involved in the wind, the latent heat flux and the longwave flux. The simulation without any correction on the stratification or meteorological parameters (*No corr*) (dotted red curve) is also shown. In each figure, the blue curve corresponds to the simulation with the stratification correction but without correction of the meteorological parameters or fluxes (*No atm corr*).

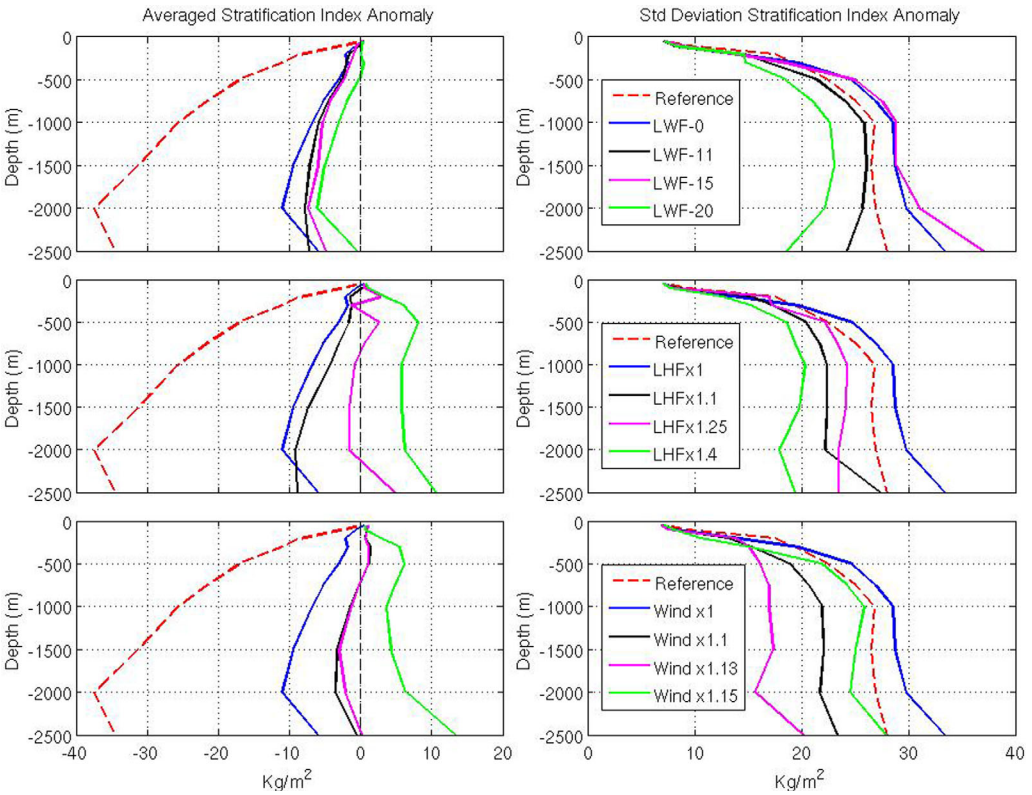

Figure 5. Vertical profiles of the average and standard deviation of the stratification index anomaly for the *No corr* simulation (without correction of initial conditions and air/sea fluxes: red dotted curve) and for simulations with different corrections of the air-sea fluxes. Top line: correction on the longwave flux (LWF), middle line: correction on the transfer coefficient of the latent heat flux (LHF), bottom line: correction of the wind. Note that the blue curve (*No atm corr* simulation) is the same for the three lines, and includes stratification corrections to the initial state and to the open boundaries using the anisotropic interpolation. Left column: anomaly (observation-model) averaged over the available profiles of the 75 CTD of the winter DEWEX-Leg1 cruise, right column: standard deviation of the anomaly.

As for the September 2012 cruise (Figure 2), the correction of initial conditions gave better performance than the *No corr* simulation, with a mean bias in winter about three times lower (but with higher standard deviations), confirming the importance of initial conditions in summer for the representation of convection through the following winter. The increase in wind or directly in the latent heat flux or in the longwave flux reduced the negative bias remaining after the implementation of correction of stratification.

On average, low-biased results were obtained with an amplification of wind of 10 to 14%. Alternatively, an increase of about 25% in the transfer coefficient C_E also provided a mean stratification similar to the observations. The constant reduction in the net longwave flux (and so in the total heat flux) seemed less efficient to reduce the bias. The different terms of the heat and water budgets over the entire period, and over autumn and winter separately are given in Table 3 for the most interesting simulations. These budgets were calculated over a box of 100x100 km^2 centered on the point 42°N, 5°E generally considered as the center of the convection region. Only grid points deeper than 2300 m were considered.

As expected, all the simulations with atmospheric corrections present a buoyancy loss integrated over the autumn-winter period that is higher than the *No atm corr* simulation. As long as only autumn is concerned, this is no longer true for *Vx1.13* which loses a little less buoyancy (−4%) because of a colder sea surface temperature as indicated by the longwave flux budget. During winter, the variability of sea surface temperature is much lower (SST∼13°C) because of the deep vertical mixing and then, in the absence of significant feedback, all the atmospheric corrections increase the heat losses. Globally over autumn and winter, *Vx1.13* and *LWF-20* have a very close budget (−0.78 kg m^{-2} day^{-1}) as the reduction of the buoyancy loss of *Vx1.13* in autumn is balanced by an increase in winter. This is because the strong winds in winter favor more intense turbulent fluxes through the increasing dependence of C_H and C_E transfer coefficients on the wind.

Table 3. Air-Sea Fluxes Averaged Over the Dense Water Formation Area (See Text) and Over the Period 15 August 2012 to 10 March 2013 (First Line), and Over Autumn (15 August 2012 to 30 November 2012) and Winter (1 December 2012 to 10 March 2013) (the Two Values Separated by a Slash on the Second Line) for the Main Simulations Discussed in This Paper[a]

Simulation	SR (W/m^2)	LWF (W/m^2)	SHF (W/m^2)	LHF (W/m^2)	Precip (mm/d)	Total heat flux (W/m^2)	Total Buoyancy Flux ($kg/m^2/d$)	Dense water (km^3)
No atm. correc	123.4	−83.6	−29.5	−143.3	2.3	−133.0	−0.727	15,398
	149.1/ 94.4	−77.4 /−89.5	−21.2 /−38.2	−132.5 /−153.5	2.2 / 2.4	−82.0 /−186.7	−0.47 /−1.0	
Vx1.13	123.4	−81.9	−28.9	−154.7	2.3	−142.2	−0.783	46,849
	149.1/94.4	−74.5/−89.1	−17.1 /−41.5	−134.4 /−175.2	2.2 / 2.4	−76.8 /−211.3	−0.45 /−1.14	
LHFx1.25	123.4	−82.2	−26.6	−169.9	2.3	−155.3	−0.863	53,090
	149.1/94.4	−75.0/−89.2	−16.5 /−37.4	−149.7 /−190.1	2.2 / 2.4	−92.0 /−222.2	−0.54 /−1.21	
LWF-20	123.4	−102.7	−27.9	−138.7	2.3	−145.8	−0.78	34,407
	149.1/94.4	−95.7/−109.1	−18.4 /−37.9	−124.1 /−153.0	2.2 / 2.4	−89.2 /−205.6	−0.5 /−1.09	

[a]Negative values correspond to a loss for the ocean. SR: solar radiative flux, LWF: longwave flux, SHF: sensible heat flux, LHF: latent heat flux, Precip: precipitation rate. The last column is the amount of dense water formed during winter (see section 3.2.3 for a description).

It can be seen that, depending on the simulation, the daily buoyancy loss in winter is between 2.1 and 2.5 times its autumn value. Finally, *LHFx1.25* presents the largest deficit of buoyancy (19% relatively to *No atm corr* compared with 5-8% for *LW-20* and *Vx1.13*).

It is noticeable that the performance of the different simulations in reproducing the winter stratification is not a simple function of the heat and water budgets integrated over the simulation. Despite very close buoyancy losses for *Vx1.13* and *LWF-20*, the stratification is lower in the first case. The simulation performed with increased wind might have a specific behavior with respect to the other simulations where only heat and/or water fluxes are increased. In greater detail, the wind increase induces an increased heat loss in winter but, conversely, in the autumn, when the mixed layer is of the order of a few tens of meters thick (typically the Ekman layer thickness), the increased shear stress produces a deepening of the mixed layer (section 5), thus inducing a lower surface temperature which, in turn, reduces surface heat losses. Simulations *LWF-15* and *LWF-20* provide similar stratification as the surface flux budget over the period is almost identical in both simulations (not shown). This is because the imposed decrease of the net flux is balanced by a reduction of the buoyancy loss, mainly through the latent heat flux resulting from a lower surface temperature during the stratified period.

The standard deviation of the stratification index anomaly (right panels of Figure 5) indicates that *Vx1.13* provides a winter stratification that is spatially more coherent than in the other simulations. In addition, it was checked (not shown) that this simulation (and *LHFx1.25*) also reduced the early autumn (September 2012) bias visible on Figure 2.

To assess the uncertainties on the volume of newly-formed dense water and on its characteristics, it is necessary to go further than the statistical validation undertaken by checking that the location of the mixed water zones was properly represented as well as the density of newly-formed water. For the first point, the concept of stratification index was used again.

The spatial distribution of the stratification index at 1000 m depth, derived first from CTD and Argo profiles measured between 30 January and 26 February 2013 and second from the main simulations selected previously, at the same points and at the same time is shown on Figure 6. The choice of 1000 m rather than larger depths was made to increase the number of Argo profiles available and because this depth gives a good indication of the presence of deep mixing. A logarithmic scale was used to assess weak values in the convection zone and strong values at its periphery. In the central area of the Gulf of Lion, mixing is well developed in the observations as well as in most simulations except *No corr*, as indicated by Figure 5. The simulation *No atm corr* produces deep mixing but it concerns fewer points than in simulations where air-sea fluxes are stronger.

In the axis of the Ligurian Sea, observed stratification was also low but mixing was not as pronounced (intermediate colors in the palette) as in the Gulf of Lion and spatial variability was high. The largest observed MLD reached 800 m in the Ligurian Sea. The model indicates these features for *Vx1.13* and *LWF-20*, while *LHFx1.25* overestimates mixing and *No atm corr* underestimates it. Finally, in the periphery of the two convective regions, stratification was much higher, in particular south of the convection zone. It may be noted

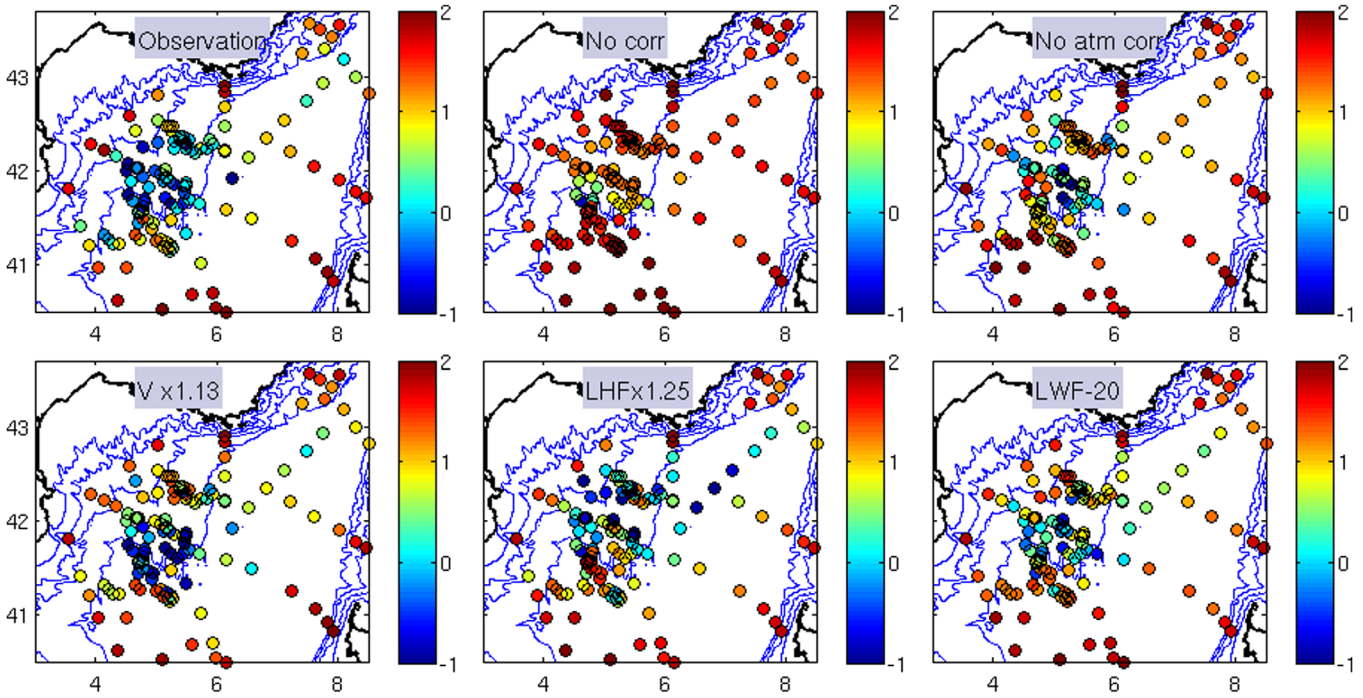

Figure 6. Decimal logarithm of the stratification index relative to 1000 m calculated between 30 January and 26 February 2013 (encompassing the DEWEX-Leg1 cruise) from observations and from corrected (stratification, wind and heat fluxes) simulations. The stratification index is expressed in kg m^{-2}. Note that blue color including cyan corresponds to very low stratification ($<$ 2 kg m^{-2}). Blue lines: isobaths 200, 1000, 2000, 2500 m.

that the transition between well mixed areas and stratified ones to the south, visible on the observations panel is generally well reproduced by simulations, especially *Vx1.13* and *LHFx1.25*. In the Gulf of Lion, north of 42°N, *LHFx1.25* is the most consistent with observations for the occurrence of deep mixing while the simulation *Vx1.13* also indicates deep mixing but less frequently than in observations.

3.2.2. Characteristics of Deep Water

An important point was to ensure that the deep water density was well represented. The comparison between observed and simulated density at 2000 m is shown in Figure 7 for all CTD profiles of the DEWEX-Leg1 cruise in February 2013 for the *No corr* and the corrected simulations. Unsurprisingly, the 4 corrected simulations show densities closer to observations than the *No corr* simulation. Coefficients of correlation with observations (indicated in the figures) also significantly increase compared to *No corr*, especially for simulations with atmospheric corrections. Discrepancies are usually less than 0.002 kg m^{-3} which is the order of magnitude of the observation errors. Moreover, two points in the observations (green dots) stand out by their high density ($\sim$29.119 / 29.121). These are also the densest points in the simulation *Vx1.13*. They correspond to stations 52 and 53 (shown by green circles in Figure 1d) sampled during the night of 17 to 18 February 2013, which were the last stations of the cruise measured in the central area of the Gulf of Lion. This is an indication that the cruise probably did not allow the entire period of convection to be monitored.

3.2.3. Assessment of the Newly Formed Dense Water

The observed and simulated density profiles at station 52 just mentioned (17 February) show mixing reaching the bottom. Observations previously made in the vicinity of these stations dated from 5 and 10 February 2013 and showed a density of 29.113 at 2000 m. A visual examination of temperature, salinity and density profiles indicates that MLD was about 1600 m on 5 February 2013 and 1900 m on 10 February 2013. The density of 29.113 at 2000 m probably corresponds to the value just before convection reached this depth. Based on these observations, it seems that, during the period of about one week between 10 and 17 February, first, mixing reached the sea floor and, second, the density increased by 0.007 kg m^{-3} (from 29.113 to 29.12) in the central area of the Gulf of Lion. This timing was checked in simulation *Vx1.13* as shown in Figures 8a and 8b which present the density of the first layer above the bottom for 10 and 17 February 2013. Between these two dates, the presence of denser water (in orange) is clear around 42°N, 5°E and between

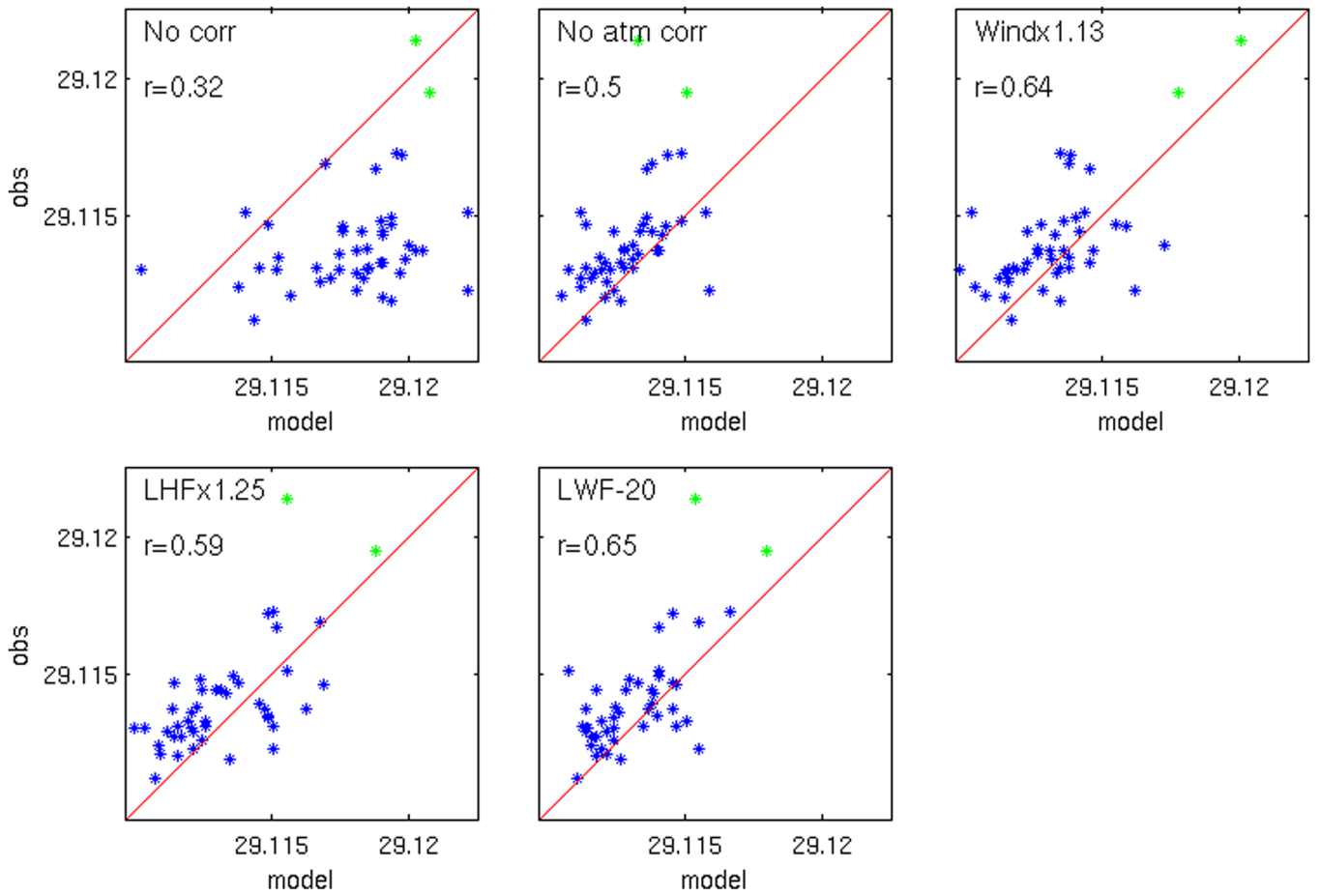

Figure 7. Comparison of observed (DEWEX-Leg1 cruise in February 2013) and simulated potential density excess at 2000 m for different simulations described in Table 2. Green dots correspond to the two observations higher than 29.118 (see text). The value of the correlation between simulated and observed densities is indicated in the figures.

the 2000 and 2500 m isobaths. It can be noted that these newly-formed dense waters are very close in density to some pre-existing water masses located south of the convection zone in regions deeper than 2500 m and to the north of the Balearic Islands, where density is the highest. These characteristics indicate the likely presence of dense water formed during the previous winter, also confirmed in the observations with densities of 29.12 - 29.121 measured close to the bottom at a few stations north of Minorca (see blue circles for positions on Figure 1d). *Durrieu de Madron et al*. [2013] observed the maximum thickness (1100 m) of dense bottom water formed during the previous winter by coastal cascading at the same place during summer 2012 (MOOSE-GE-2012 cruise). A year of presence of a large amount of coastal dense water formed during winter 2011-2012 in the Balearic Sea is a point that should be further investigated.

After the last surface to bottom CTD observations in the convection zone on 17 February 2013, the model documented the effect of the next strong wind episode that occurred in the region from 23 to 26 February 2013. This event induced an additional densification of the already mixed water column and a horizontal expansion of the mixed region (see bottom density on 28 February on Figure 8c). It also produced dense water formation on the Gulf of Lion shelf, followed by cascading in the Cap de Creus canyon at the southwestern end of the Gulf of Lion's shelf, which reached the 2000 m isobath on 28 February (note that a first episode of cascading visible in Figure 8b occurred from 12 to 16 February). Dense water formed by convection reached its maximum density at 29.124 kg m^{-3} but this value was limited to an area of the order of 100 km^2 in the model. A dense water budget was calculated by considering areas deeper than 1500 m and north of 41°N (including the Gulf of Lion and the Ligurian Sea) to avoid counting dense coastal water that did not reach the deep basin or the large volumes of old dense water present mainly north of the Balearic Islands.

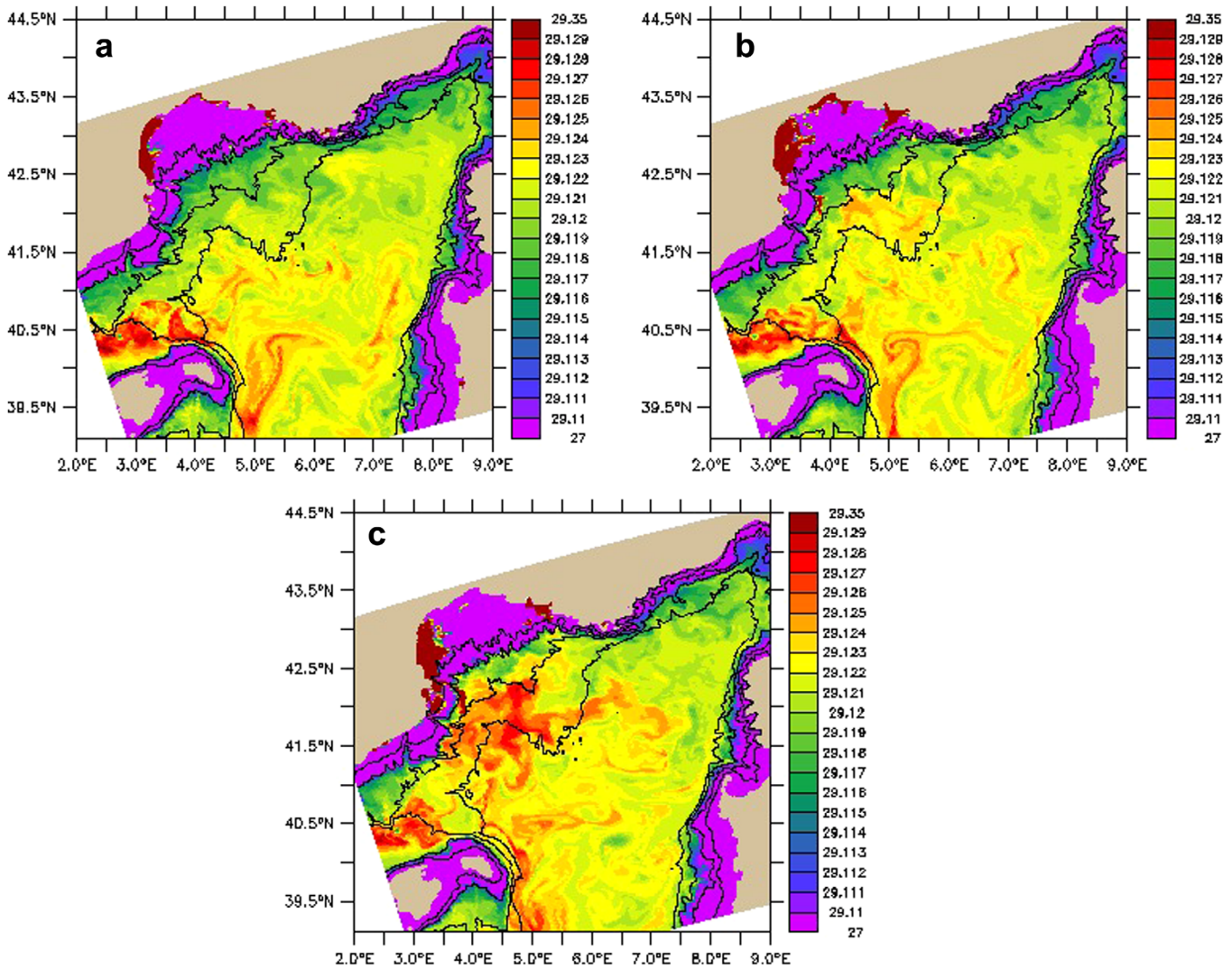

Figure 8. Spatial distribution of bottom potential density excess (kg/m^3) simulated with *Vx1.13* for (a) 10 February 2013, (b) 17 February 2013, (c) 28 February 2013. Isobaths: 200, 1000, 2000, 2500 m. Note the saturation of the palette for low and high densities.

The difference in the volume of dense water between 1 September 2012 and the end of convection (10 March 2013) is shown in Figure 9 for the last selected simulations with and without atmospheric correction and for different density classes. All simulations with atmospheric corrections indicate the replacement of a water volume of density lower than 29.113 by water denser than this threshold (all the classes lower *resp*. larger than 29.113 present a decreasing *resp*. increasing volume). Conversely, the volume of water with density larger than 29.113 decreased in the simulation without correction of the initial state *No corr* (not shown). The newly-formed water volume varied from 15,000 km^3 for the simulation *No atm corr* to 34,000, 47,000, and 53,000 km^3 respectively for the simulations *LWF-20*, *Vx1.13* and *LHFx1.25* (Table 3). Despite the buoyancy budget of the simulations *Vx1.13* and *LWF-20* being almost identical, the volume of dense water formed was 36% higher in the first simulation. Likewise, the buoyancy budget of the simulation *Vx1.13* was only 7.7% higher than the *No atm corr* one, while the volume of newly-formed dense water was three times higher. This is supplementary evidence that the time-integrated buoyancy budget over the autumn - winter period is far from being an indicator of the volume of newly-formed water, even if the model starts from the same initial state in summer.

Finally, to better constrain the volume of dense water, it can be noted that the simulation *LWF-20* does not produce water as dense as in simulations *Vx1.13* and *LWFx1.25* nor significant cascading of coastal water at large depths. This is in contradiction with temperature and current speed observations at 1000 m in the

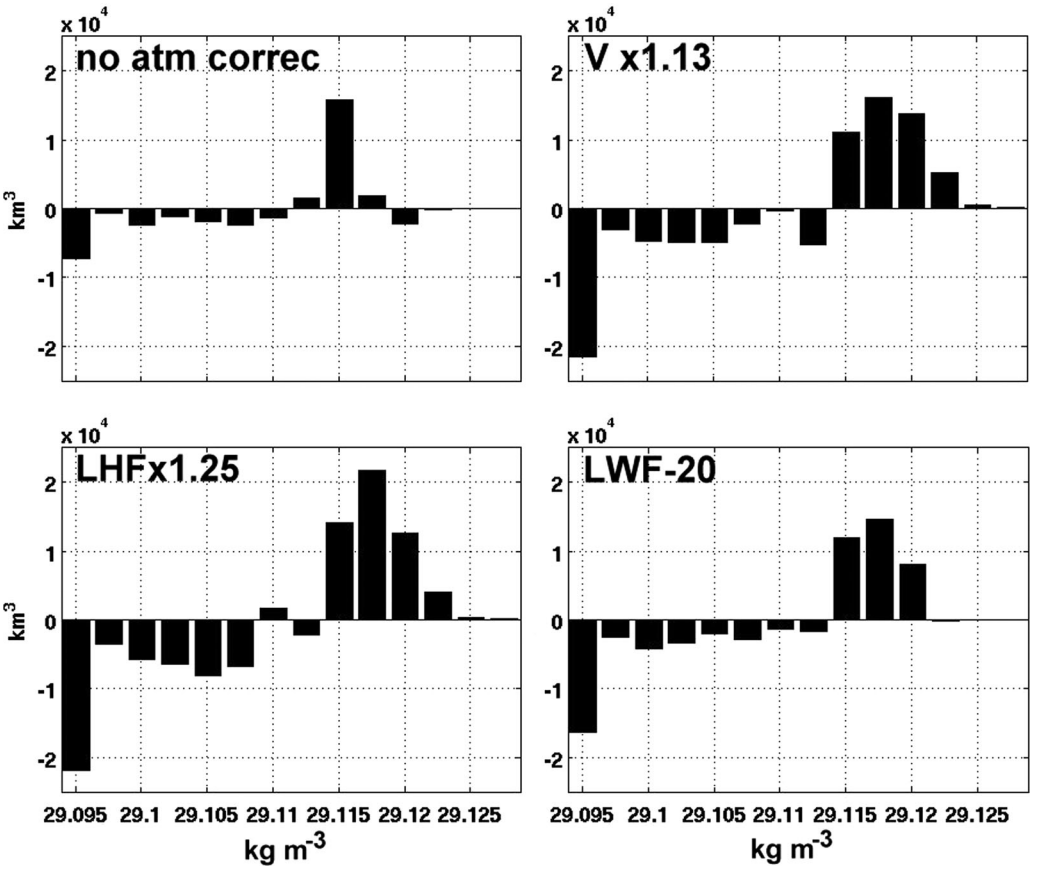

Figure 9. Budget of dense water (in km^3) for different intervals of density calculated by difference of volume at two dates (10 March 2013 to 1 September 2012). The first class of density represents the volume of water lighter than 29.096 kg m^{-3} and the last class the volume of water denser than 29.126 kg m^{-3}.

Lacaze-Duthiers canyon (not shown) indicating that the winter 2012-2013 was one of the few times that deep (> 1000 m) dense shelf water cascading occurred since 1993. If the simulation *No atm corr*, which is too biased, is also removed from the pool of the most realistic simulations, the remaining simulations indicate that the volume of newly-formed dense water is about 50,000 km^3 which is equivalent to a mean annual production rate of 1.6 Sv. This amount is in the range of the estimate of 1.84 $\pm$ 0.48 Sv for the 29.11 kg m^{-3} density water class by *Waldman* (pers. comm.) based on optimal interpolation of CTD profiles. In the rest of the paper, the simulation *Vx1.13* is selected as it generally performs well to reproduce the timing of convection, the area affected by convection and the characteristics of dense water.

4. Evolution of Stratification From Summer to Winter

4.1. Summer Stratification

The stratification index relative to 200 m for each CTD profile of the August 2012 MOOSE cruise is shown in Figure 10a. During this summer period, near the surface, three water masses are organized along the north - south direction. First, south of 41.5°N, light surface Atlantic waters from the Algerian basin (high T, low S, strong stratification index > 120 kg m^{-2}) are the least modified / most recent of the 3 Atlantic water masses. Second, between 42°N and the slope, the densest surface waters (with a low stratification index < 80 km m^{-2}) corresponding to the upper part of the isopycnal doming preconditioning convection are the most modified / oldest of the 3 water masses. Finally, to the north, along the slope, part of the general circulation of the basin (not visible for every transect of the cruise), waters with intermediate stratification and intermediate density are older than the first ones because of their longer residence time in the western basin (longer distance covered along the cyclonic path of the surface Atlantic water). Potential density profiles typical of the first two water masses (the most important ones for the following) are plotted in Figure 10b. At the

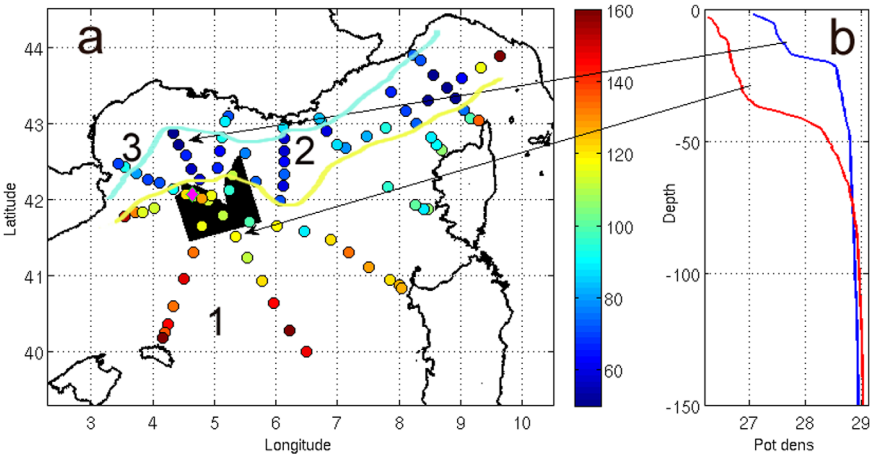

Figure 10. (a) Stratification index relative to 200 m calculated for each CTD profile of the August 2012 cruise. (b) Potential density vertical profile observed at the two points indicated by arrows. The black area corresponds to the area where the budget of Figure 16 was calculated (section 5). The magenta diamond is the location of the LION buoy. The freehand lines and the numbers 1, 2, 3 give an approximate indication of the three surface water masses discussed in section 4.1.

time of the cruise, the LION buoy (42.06°N 4.64°E indicated by a magenta diamond on Figure 10a) was located in the gradient between these two water masses.

4.2. Surface Layers in Autumn at the Center of the Convection Zone

The observed and simulated temperature evolution over the first 150 m under the LION meteorological buoy are compared in Figure 11 with a focus at 20 m depth. The simulation reproduces the temperature variations in the first tens of meters during autumn with successions of cooling and warming events superimposed on a general cooling trend. For example, in October, a warming of about 2°C at 20 m is observed in the first half of the month followed by a return to ~20°C and then a sudden drop of 4°C at the end of the month. In November, the MLD starts to deepen significantly but warming of the surface layer still occurs until the event of the end of November that definitively breaks the stratification of the 0-150 m surface layer. Early December can be considered as the transition between autumn and winter.

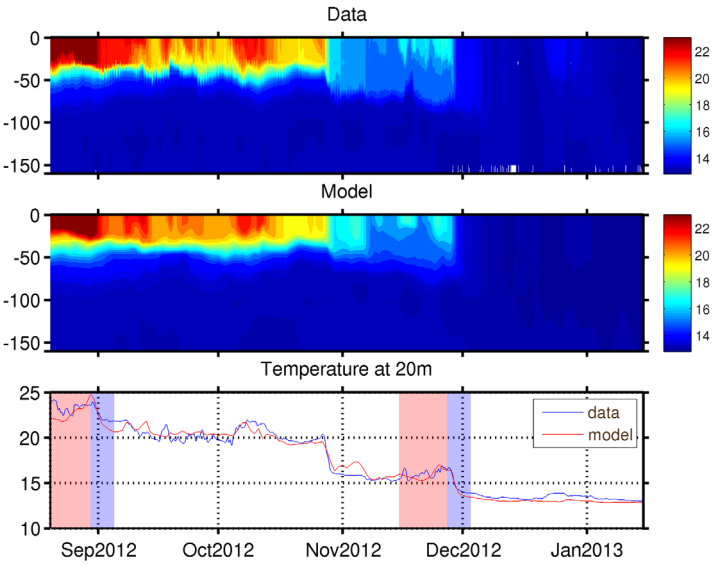

Figure 11. Time series of 0–150 m potential temperature at the LION buoy: (top) measured, (middle) simulated. (bottom) Comparison of measured and simulated temperature at 20 m. The pink and blue vertical bars correspond to events discussed in section 5. Ticks on the horizontal axis correspond to the first day of the month indicated.

4.3. Convection in Winter

The evolution of temperature simulated at the grid point corresponding to the LION buoy is now shown for the whole water column (Figure 12). After December, the surface layers continued to cool until their potential density became larger than that of the Levantine Intermediate Water. During this pre-convection period, the temperature of the surface water was the lowest of the year, near 12.8°C for the first two weeks of January. This water mass was then consumed by mixing in one week around 25 January. Mixing with the LIW produced an increase of temperature (reaching 13°C) and salinity of the surface layers. The MLD then increased rapidly as the stratification under

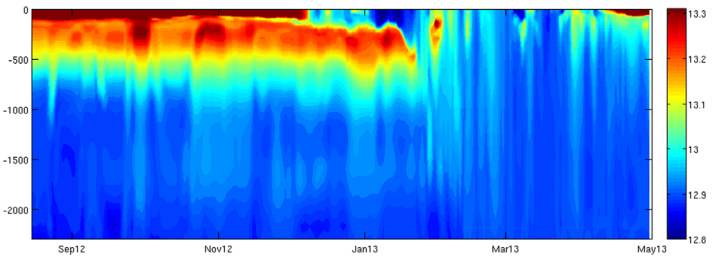

Figure 12. Evolution of the vertical profile of temperature simulated at the grid point corresponding to the LION buoy (see also Figure 11 for the surface layer in autumn). Ticks on the horizontal axis correspond to the first day of the month indicated.

the LIW was low. Convection then appeared intermittent with short events of restratification, horizontal heterogeneities also playing a role in the observed variations of temperature. Around mid-February, convection reached the sea floor as mentioned in section 3.3. After a last convection event around mid-March, restratification by warmer water appeared in the first hundred meters.

Because of the thickening of the MLD, the front between the convective layer and light water became baroclinically unstable. As shown on an ocean color image of 19 February 2013 (Figure 13a), meanders developed and light and dense waters (respectively rich and poor in chlorophyll) interpenetrated. The size of these structures was rather well represented by the numerical model, as shown by the surface potential

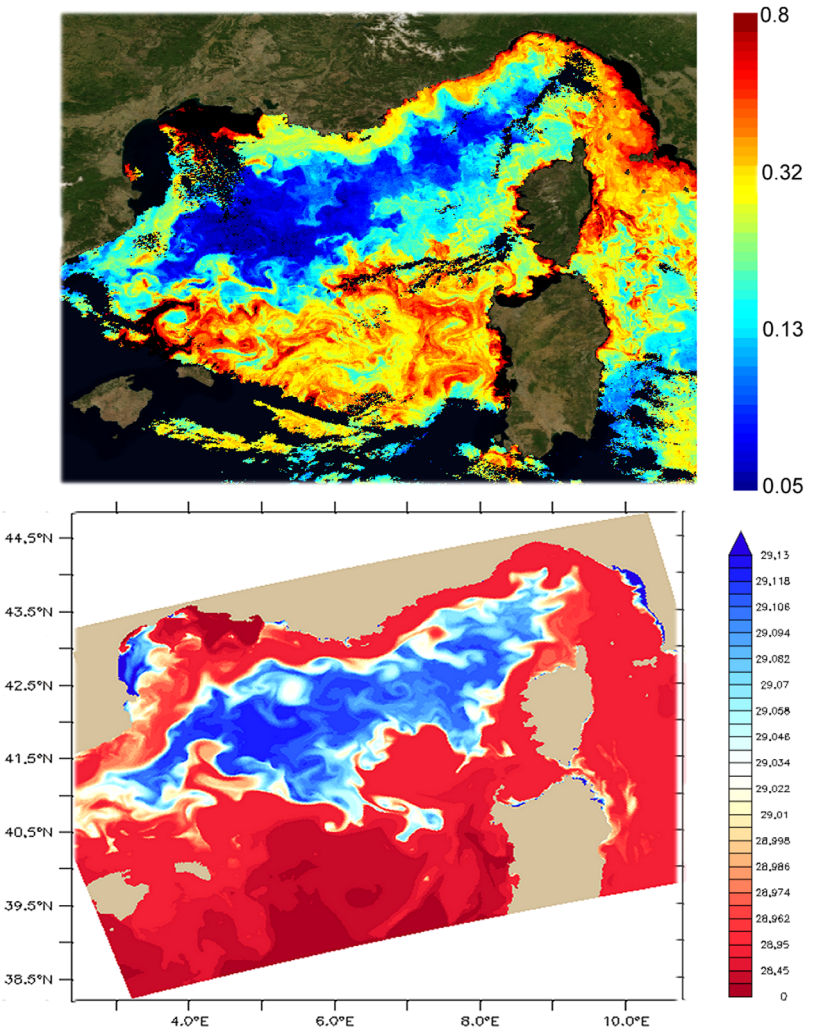

Figure 13. (top) surface chlorophyll concentration in mg m^{-3} from MODIS (source : MyOcean) for 19 February 2013. (bottom) sea surface density simulated for the 19 February 2013 with the *Vx1.13* simulation. Note the use of irregular scales. Note also the presence of dense water along the northern coast of Sardinia and the coast of Tuscany. The conjunction of shallow water and strong wind is responsible of dense water formation in the simulation. The non-inclusion of rivers in these regions could lead to an overestimation of this process.

density map averaged over the same day (Figure 13b). In both cases, structures of about 20 km can be seen at the periphery of the mixed patch together with filaments of about 10 km in width developing inside the patch. The 1 km model resolution appears relevant to represent the wide range of scales present in the convective area.

5. Processes Affecting Vertical Mixing in Autumn and Winter—Heat and Salt Budget

The processes modifying the stratification and leading to the formation of dense water are now studied and quantified through the autumn winter period. First, the history of the water column destratification is compared to the integrated effect of air sea fluxes (Figure 14) at the model grid point corresponding to the LION meteorological buoy close to the center of the convection zone. This point was chosen to link with the evolution of the stratification shown in Figures 11 and 12. The lower panel of Figure 14 displays the surface buoyancy flux. The upper panel compares the evolution of the stratification index relative to the sea bottom with the cumulated surface buoyancy flux (whose curve was shifted to start with the stratification index of 15 August 2012). When the two curves are parallel, the variations of the stratification index are induced only by the air sea fluxes. In other cases, advection cannot be ignored. If the stratification index decreases faster than the cumulated surface buoyancy flux, advection destratifies and vice versa. When the stratification index reaches 0, the water column is mixed down to the reference depth, here the bottom. A supplementary buoyancy loss (starting in mid-February here) produces a densification of the water column without further decrease of the stratification index. The two curves can no longer be compared until the restratification begins (about mid-March here).

Figure 14 allows two regimes to be distinguished. Before 1 December, the stratification index undergoes stronger variations than suggested by air sea fluxes. Integrated over autumn, the decrease of the stratification index (red curve) is stronger than the decrease due to surface fluxes (blue curve). From December (winter period), the stratification index decreases more regularly. In contrast to the autumn period, the decrease of the stratification index is slower than imposed by surface fluxes.

Going into detail for autumn, periods of increased stratification can be observed (pink bars) which correspond to temperature increases observed in the MLD (Figure 11). These increased stratification events are characterized by surface buoyancy fluxes close to 0 (Figure 14, bottom). This is true for the two events highlighted in pink and also for other, less marked events between them. The first strong wind event with strong buoyancy losses following each of these high stratification periods is accompanied by a sudden cooling and a sudden drop of the stratification index (see periods in blue on Figures 11 and 14). A vertical section oriented north-west to south-east (Figure 15), simulated before and after the wind event marked by the second blue bar of Figures 11 and 14, indicates the position of the three surface water masses identified in Figure 10 and the subsurface structure of the density dome which preconditions winter convection. The density gradient bounding the isopycnal doming is not symmetric on its northern and southern sides. On the northern side, the slope of the isopycnals is steep as they are constrained by the topography. The Northern Current, maximum at the surface and several hundred meters thick, is

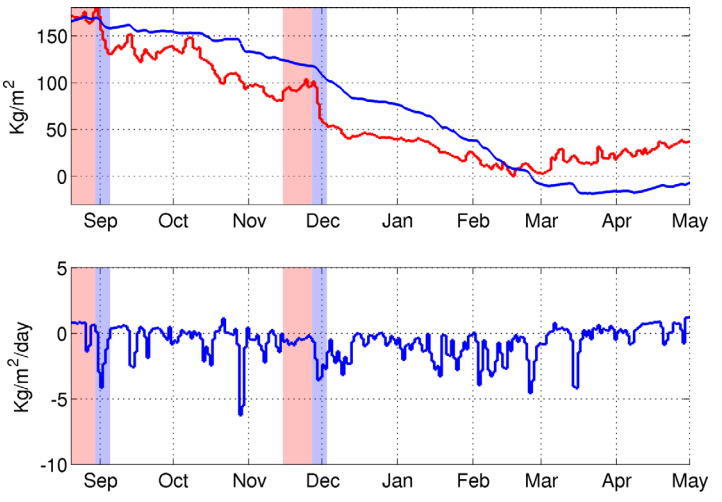

Figure 14. (bottom) surface buoyancy flux simulated at the LION buoy; (top) stratification index relative to the bottom simulated at the LION buoy (red), cumulated surface buoyancy flux shifted to start with the value of the red curve on 20 August 2012 (blue). The pink/blue vertical bars correspond to stratification / destratification events discussed in section 5. Ticks on the horizontal axis correspond to the first day of the month indicated.

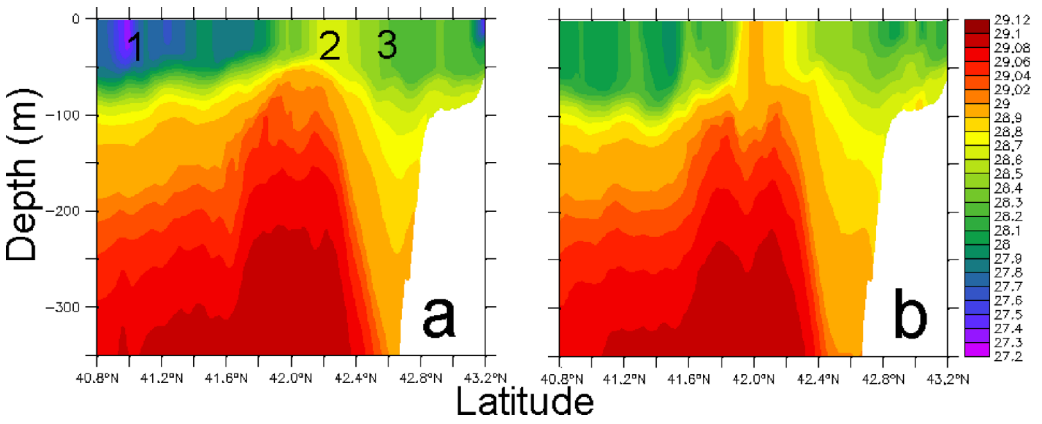

Figure 15. Vertical south-north section of density simulated for (a) 28 November 2012 and (b) 2 December 2012. The numbers indicate the position of the three surface water masses identified in Figure 10: 1 for the Atlantic waters, 2 for the dense water of the isopycnal doming, 3 for the along slope current.

associated with this density gradient. On the southern side of the doming, there is no bathymetric discontinuity; the density gradients of the North Balearic front concern the surface layer (100-200 m), which is not known to be associated with any important geostrophic current [*Millot*, 1987]. This front is characterized by strong distortions [*Taupier-Letage and Millot*, 1988]. Its position is known to be affected by seasonal variations. During winter, because of the densification of surface waters by the frequent wind events, the front is located to the south, typically around 41°N. During summer, because of the seasonal stratification and the less frequent north wind events, the light waters from the south shift to the north [*López-García et al*., 1994].

Figure 15 reveals that the surface front also moves on short time scales, in response to the wind variability.

1. When the north wind is weak, a thin layer (∼MLD) of light Atlantic waters spreads northward over the dense water. Surface dense waters (region 2 on the figure) are then confined to the north in a narrow band along the Northern Current (see Figure 15a where surface dense waters are even slightly shifted on the northern side of the subsurface density dome). The MLD in these dense waters is shallow as its vertical extent is constrained by the isopycnal doming (typically the blue profile of Figure 10b). The mixed layer thickens southward and the density decreases (see region 1 in Figure 15a and the typical red profile of Figure 10b for observations in summer). During such situations, the LION buoy is in the relatively light waters as in Figure 10a. These periods correspond to increases of the stratification index of 10-20 kg m^{-2} at the buoy (the pink bars on Figure 14),
2. When the north winds blow, the Ekman transport pushes the surface waters south-westward. As an example, the simulation shows that, during the 4 days between 28 November and 2 December 2012 (second event underlined in blue on Figure 14), the front was shifted southward by 30 km (see evolution between Figures 15a and 15b). Therefore, during such periods, the sudden decrease of the stratification index at the buoy reflects not only a local cooling but also the return of dense water near the surface. In the same way, the temperature variations in the MLD in Figure 11 largely reflect the displacement of the front.

The northward displacements of the front are reduced after December as the low-wind periods are short and the mixed layer has become thick ($>$ 100 m) and is so able to resist the advance of the light waters from the south.

To conclude, Figure 14 indicates that, in this region supposed to be relatively isolated inside a cyclonic gyre, advective processes seem to be important compared with the impact of surface buoyancy losses in terms of changes in the vertically integrated buoyancy. The main trend of these processes on buoyancy is opposite in autumn (stratified period) and in winter (mixing period).

The cumulated contribution of advective and non-advective fluxes to the temperature and salinity budget was calculated by considering 3 layers (Figure 16): the surface layer (0-150 m), the intermediate layer (150 – 600 m) and the deep layer ($z > 600$ m). This budget is no longer calculated over a single model

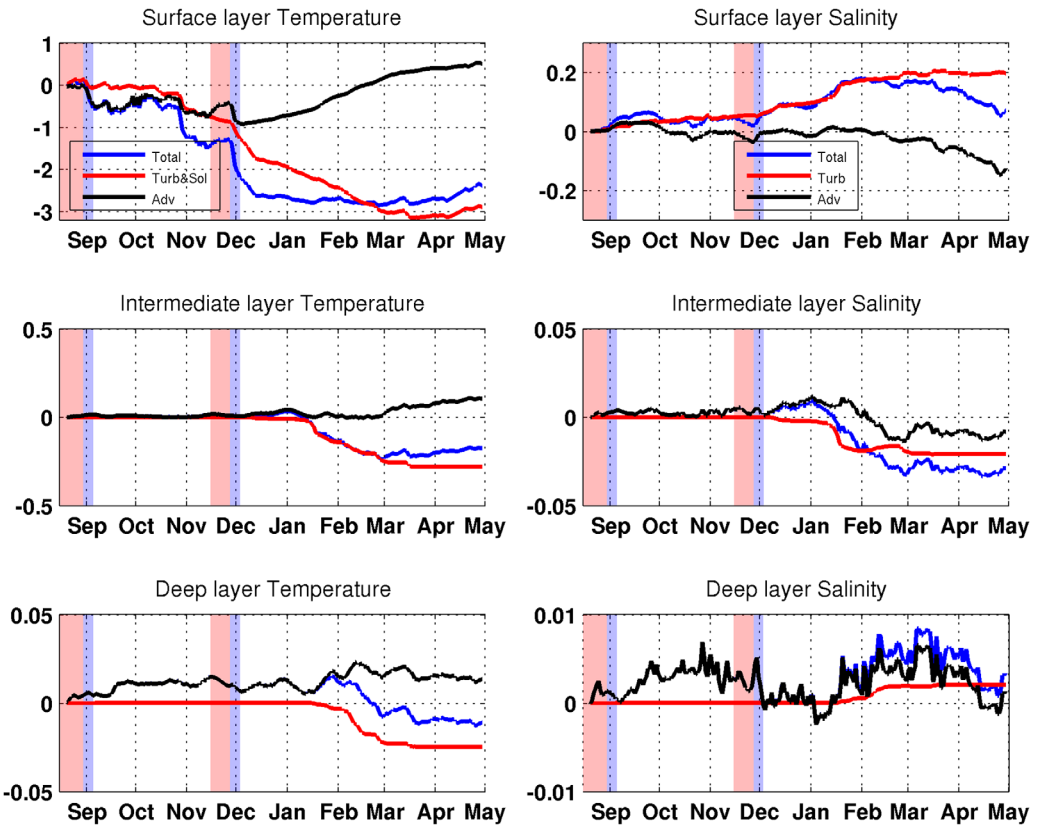

Figure 16. Time cumulated evolution of average temperature (°C) and salinity (psu) for the surface (0–150 m), intermediate (150–600 m) and deep layer (> 600 m) inside the box of Figure 10. The different curves correspond to different processes: black: advection, red: turbulent (and solar for temperature), blue: total. The accumulation period starts at the model initialization. Note the different vertical scales used for the three layers.

grid point as in Figure 14 but over a 100x100 km^2 area centered on 42°N, 5°E, whose grid points shallower than 2300 m have been excluded to avoid the influence of the slope current (see black box on Figure 10). The area in the black box of Figure 10 is entirely affected by deep convection in mid-February. Furthermore, it has been checked that the trends of Figure 14 found at the LION buoy were also true at the scale of this box. For each layer, the budget of non-advective fluxes (turbulent + solar hereafter Turb&SolT and TurbS) and advective fluxes are provided at each model time step by the numerical resolution of the temperature and salinity model equations. At the sea surface, the Turb&SolT and TurbS fluxes correspond to the heat and water fluxes (equations (2) and (4)) while at the levels below the solar flux penetration depth, they correspond to the temperature and salinity turbulent fluxes. The budget of the 3 layers is:

$$Turb\,\&\,SolT_1 = Q_{net} - \left(K_H \frac{\partial T}{\partial z}\right)_{bottom} \quad ; \quad TurbS_1 = Q_E + \rho_w L\,P - \left(K_H \frac{\partial S}{\partial z}\right)_{bottom} \tag{9}$$

$$Turb\,\&\,SolT_{2,3} = \left(K_H \frac{\partial T}{\partial z}\right)_{top} - \left(K_H \frac{\partial T}{\partial z}\right)_{bottom} \quad ; \quad TurbS_{2,3} = \left(K_H \frac{\partial S}{\partial z}\right)_{top} - \left(K_H \frac{\partial S}{\partial z}\right)_{bottom} \tag{10}$$

Subscript 1 refers to the surface layer, 2 to the intermediate layer and 3 to the deep layer. K_H is the vertical diffusivity (z dependent), subscripts *top* and *bottom* refer to the extremities of each layer. Note that, integrated over the whole water column, the budget reduces to the surface fluxes as the fluxes at intermediate levels cancel each other out and the fluxes at the sea bottom are zero.

In autumn, advection is restricted to the 0-150 m layer at most, as evidenced by curves close to 0 for the other two layers. Concerning the events characterizing the displacement of the front, it can be observed that the two decreases of the stratification indicated by blue bars on Figure 14 are associated with sudden

changes of the advection trend (mainly a cooling, see Figure 16). Note that another event of the same type is visible in late October at the scale of the large box (Figure 16) but not at the LION buoy (Figure 14). Figure 16 shows that the advection budget in the surface layer over each round trip of the front is not zero. Integrated over time, advection tends to cool and densify the water column as the temperature decrease of the water mass is higher when the front shifts to the south than the inverse trend when the front goes back to the north. These events are also marked by a sudden deepening of the mixed layer (Figure 11). Schematically, the surface current nearly parallel to isopycnals (and isotherms) before the wind event, is dominated during the wind by the vertically sheared, and in some places, cross-isotherm Ekman component. This motion advects dense water over light water or steepens the front in a region defined by the geometry of the isopycnals and the Ekman transport direction. The resulting Ekman buoyancy flux creates a layer with negative potential vorticity. Slantwise convection develops and deepens the mixed layer. For example, the MLD increases from 40 m to 120 m in 4 days between 28 November and 2 December (Figures 11 and 15 at 42°N). Such large increases of the MLD exist along the western and southern surface fronts bounding the density dome and also contribute strongly along the Northern Current in the Ligurian Sea where the wind blew from the north-east during a large part of this period. This Ekman buoyancy flux is combined with surface buoyancy fluxes, which are enhanced on the warm (south) side of the front. On 28 November, the simulated daily non-solar surface flux is 1097 $W\,m^{-2}$ and 705 $W\,m^{-2}$ at two points 45 km apart, respectively south and north of the front. This difference is due to an SST difference of about 2.5°C. This process contributes to the deepening of the mixed layer at the border between regions 1 and 2 of Figure 15 and then to the widening of region 2.

The impact of wind events on the advective component of the salt budget is positive (blue bars on Figure 16) but very low compared to the impact on temperature. The salt budget in the surface layer is dominated by evaporation, which induces a slow increase of salinity (∼0.1 from September to December). It is noteworthy that, until 10 October, as far as density is concerned, the impact of surface fluxes on salinity is stronger than on temperature, as the heat budget is balanced on average (heat losses by non-solar flux balancing solar heating).

From December, the advection acts to stratify the water column as was deduced from Figure 14. The impact of advection on density is dominated by the temperature. Advection mainly concerns the surface layer (Figure 16) with a regular warming trend opposite to the effect of surface buoyancy fluxes, which produce increases in cooling and salinity.

In mid-January, convection mixes the intermediate layer with the surface layer. The effect of entrainment of intermediate waters in the mixed layer is to decrease their mean temperature and salinity as the maximum of their properties is diluted by mixing with surface water. The consequence for the surface layer is an increase of salinity but no clear signal on temperature as this entrainment is produced by a long event of strong surface heat losses counterbalancing the vertical input of heat from intermediate waters.

The deep layer is progressively mixed from the end of January. After 10 February, the surface fluxes allow the whole water column to cool without significant changes of salinity. The contribution of advection to the budget of intermediate and deep water is small and variable. In detail, the slight increase of temperature and salinity in intermediate waters in March could be related to a beginning of restratification during this period, which is most often calm (except one strong event) and thus favorable to restratification. The study of the restratification phase during the post convective period is beyond the scope of this paper as the present simulation is too short to represent it.

The analysis of the mass budget calculated with the model gives an estimation of the contribution of advection compared to surface fluxes in autumn and winter. Integrated from September to the beginning of December (autumn) in the surface layer, turbulent+solar fluxes represent about 60% of the total fluxes and advection 40%. From the first days of December to the beginning of March (winter), the stratifying effect of advection represents 58% of the destratifying effect of surface fluxes. Following *Visbeck et al*. [1996] and Lascaratos and Nittis [1998], we calculated the time, t_{eddy}, (equation (11)) necessary for the baroclinic eddies developing around the convection area to stop the development of convection and we compared it to the time, t_{mix}, of development of the mixed layer depth subjected to surface fluxes only.

$$t_{eddy} = 12\left(\frac{r^2}{B}\right)^{1/3} \tag{11}$$

r is the radius of the mixed patch and B the average buoyancy loss in $m^2\ s^{-3}$. As the mixed patch is not circular (Figure 13), its radius is not easy to determine. For the region of the Gulf of Lion, we gave an estimation of between 50 and 100 km, leading to values between 37 and 49 days for $B=1.3\times10^{-7}$ (the buoyancy loss averaged between 1 December and 1 March). Following *Lascaratos and Nittis* [1998], the evolution of the MLD (h) subjected to surface fluxes only was calculated from:

$$\frac{\partial h}{\partial t}=\frac{B}{N^2\,h} \tag{12}$$

where N is the Brunt-Vaisala frequency taken from the potential density profile on 1 December. Integrating equation (12), we obtained $t_{mix}=45$ days for the development of the MLD down to 2000 m with the same value of B as above. The fact that the two time constants are close means there is strong competition between these vertical and lateral processes, as reflected by the slow decrease of the stratification index compared to the surface buoyancy (Figure 14) or by the temperature budget of Figure 16. Complete mixing occurred around mid-February (75 days after 1 December) while surface fluxes alone would have mixed the water column about one month earlier. It was noticed that the intermittencies of surface forcing seemed to play a role in the duration taken for the complete mixing of the water column. After the periods of low surface fluxes and despite the beginning of new strong wind periods, the stratification index at the scale of the box remained constant or sometimes increased slightly, revealing the development of baroclinic eddies that delayed the further mixing.

6. Discussion

Sensitivity studies have shown that the correct representation of the mixing induced by convection, for example the density of newly formed water and its volume, requires a correct representation of the stratification in the initial state of the model. Here, with an initial state taken 6 months before convection, the chronology of mixing and the dense water formation have been correctly simulated. The accuracy of air sea fluxes is more often presented as a priority than is the accuracy of the initial state. These two points are related as the too-strong stratification in the *Nocorr* simulation would require increased heat losses to produce correct convection. In a first approach, the difference of the stratification index between the simulation and the observations at the initial state of the model can be related, through equation (13), to the supplementary (positive or negative) surface buoyancy flux (left-hand side of equation (13)) that should be applied during a time interval Δt to consume the excess of buoyancy contained in the initial state (or reduce its consumption when buoyancy is missing) and then, after Δt, simulate the observed mixing down to level Z.

$$\alpha\,\frac{\Delta Q_{net}}{C_p}+SSS\beta\left(\frac{\Delta Q_l}{L}+\Delta P\,\rho(0)\right)=\frac{F_{obs}(Z)-F_{\mathrm{mod}}(Z)}{\Delta t} \tag{13}$$

where SSS is the surface salinity, α is the thermal expansion coefficient and β is the saline contraction coefficient. The first (respectively second) term of the left hand side of equation (13) relates to the modification of temperature (respectively salinity) by air-sea fluxes. In the case of the *NoCorr* initial state, destroying the stratification excess between the surface and 1500 m would require a cumulated deficit of surface buoyancy flux of 40 $kg\,m^{-2}$ (Figure 2). This deficit is equivalent to an additional latent heat flux of $-40\ W\,m^{-2}$ for the six months of simulation (calculated from equation (13) by transferring the buoyancy on this term and keeping the other components of the heat and water budget unchanged).

Such an artificial increase of the heat loss should allow convection to be simulated with dense water volumes that are potentially realistic but with a bias on the density of these waters due to the bias of the initial condition. The increase of heat losses intended to produce convection could therefore lead to a drift of the surface stratification, in the permanently stratified regions, which could gradually deteriorate the water mass properties in the basin, their coherence with the inflowing waters at Gibraltar and finally some characteristics of the general circulation.

Another benefit of using a correct initial state is that it allows the atmospheric flux data sets to be evaluated even though, in our study, it was difficult to discriminate between some of these data sets. A perspective of this study would be to simulate a succession of several years for which observations of the deep water

properties were available. Successive changes of these properties observed during recent years would be an asset for this assessment [*Schroeder et al*., 2016].

The resolution of the horizontal grid used here is 1 km. This resolution allows mesoscale structures larger than 8 km (corresponding to 8 grid points) to be represented, which are therefore close to the winter Rossby deformation radius. Figure 13 shows similarities between the simulation and a satellite image concerning the size of structures bounding the mixed patch. It supports the existence of quasi permanent exchanges between the mixed patch and its periphery, which significantly contribute to the heat budget of the surface layer (Figure 16). Considering that the simulation represents the chronology of convection and the evolution of water mass properties, it is likely that the kilometric resolution is suitable to reproduce a wide range of spatial scales that significantly contribute to exchanges through the mixed patch.

The representation of fronts is also favored by the high resolution of the model. It has been shown that, in autumn, the simulation reproduces the temperature evolution in the mixed layer very closely (Figure 11) and that this evolution is strongly linked to the dynamics of the North Balearic front in relation with the wind. When the wind has a down-front component, a wind-driven buoyancy flux equal to the product of the down-front wind stress by the lateral buoyancy gradient is created. The Ekman flow advects dense fluid over the light one, triggering convective overturns [*Taylor and Ferrari*, 2010]. Below the mixed layer, the Ekman buoyancy flux may also create a negative potential vorticity despite a stably stratified vertical density profile, by increasing the horizontal density gradient. In this case, slantwise convection is triggered, reducing the tilting of isopycnals to cancel the potential vorticity. A deeper analysis of our simulation could be performed in a further study to identify and quantify these processes along the different fronts surrounding the convection zone and at different stages of the development of the mixed layer. These frontal processes induced by the wind are intensified by the increase of the surface fluxes by the high SST of the Atlantic waters (section 5). The addition of these two processes, Ekman buoyancy flux and surface buoyancy flux, contributes to the fast deepening of the MLD and to an increase in the size of the area preconditioned for winter convection. *Bosse* [2015], using glider sections and high resolution modeling in the same region, also showed the role of the wind in the loss of buoyancy and the destruction of potential vorticity along the Northern Current.

As discussed by *Thomas* [2005], the wind-driven buoyancy flux is proportional to the resolution of the model. It can probably be concluded from the good agreement of the simulation and observations in Figure 11, that the horizontal resolution of the model allows the impact of this process on the stratification to be accurately represented. It has also been noted that the performance of the different simulations presented in section 3.2 in reducing the stratification bias is not a simple function of the surface buoyancy budget. The success of simulation *Vx1.13* compared to *No atm corr* despite a weak increase of heat fluxes could be due to an increase of the Ekman buoyancy flux. This is supported by the comparison with the other simulations (not shown), indicating that, despite its surface buoyancy loss in autumn, which is the lowest one of all the simulations, *Vx1.13* is the simulation that best reproduces the complex evolution of the surface layer temperature in autumn as well as the thickening of the MLD during the event of late October presented in Figure 11. The impact of the Ekman buoyancy flux has been highlighted for a few events but, as mentioned earlier, this process deserves more investigation, which falls outside the scope of this paper.

To finish with the benefits of high resolution, *Damien* [2015] has shown that the 1 km resolution in this region also allows us to realistically simulate the different kinds of submesoscale coherent vortices (SCV) formed during convection with radius ∼5km and with lifetimes of several months, such as observed by *Testor and Gascard* [2006]. These SCV have been found to be responsible for 30–50% of the export of the new deep water out of the convection zone [*Testor and Gascard*, 2006].

7. Conclusion

The MOOSE-GE cruise, which describes the temperature and salinity gradients between the convection zone and the topographic slope every summer with a resolution of the order of 20-30 km, appears relevant for constructing 3D temperature and salinity corrections to improve the initial state of a high resolution regional model of the north-western Mediterranean, which is then able to reproduce the evolution of the mixed layer closely in autumn and winter. This seems to indicate that, with precise initial conditions and

atmospheric fluxes time series, oceanic convection is predictable at the scale of several months. This result would be interesting to explore with other years and in other regions.

Once the initial stratification has been corrected, atmospheric forcing has to be refined. The comparison between simulation and observations on all available winter CTD indicates better precision when the wind is increased by 13% or alternatively with an increase of about 25 % in the transfer coefficient used in the latent heat flux formulation. It is noteworthy that, in the model, the air-sea flux budget on the autumn winter period does not, by itself, explain the intensity of convection or the volume of newly-formed dense water. Despite the fact that the buoyancy budget of the simulation with the corrected wind was only 7.7% higher than in the simulation without atmospheric correction, the volume of newly-formed dense water was three times higher. This result illustrates, first, the importance of knowing each component of the heat and water budget accurately, and, second, how important it is to deepen our understanding of the mechanisms leading to the volume of newly-formed dense water beyond the over-simple time-integrated buoyancy budget diagnosis. For example, increasing wind does not simply strengthen the heat loss and evaporation but also produces Ekman buoyancy flux when interacting with the North-Balearic front in autumn. This process, the intensity of which is dependent on the horizontal resolution of the model, added to the intensification of the surface buoyancy flux on the warm side of the front, favors the convection preconditioning.

During winter, and more precisely during the convection phase, lateral advection tends to restratify surface waters. Restratification has most often been highlighted after the end of convection. Here, we suggest that, integrated over the winter, the stratifying effect of advection through the mixed patch could represent 58% of the destratifying effect of surface fluxes. Processes at the origin of this advection need to be better described, in particular their horizontal scale (from submesoscale to mesoscale to large scale). In the future, this budget could be calculated in boxes of different sizes but it is noteworthy that the importance of advective processes found at the LION buoy (Figure 14) was also found at the scale of the box.

The convection zone is thus subjected to 3D processes with opposite effects on its stratification in autumn and winter. Although these processes characteristic of the two seasons, more or less cancel each other out at the annual scale, they have a strong impact on the chronology of events, on the volumes of the newly formed water and on the lateral mixing of the water upwelled by convection. In the same way that *Herrmann et al*. [2008a] compared an eddy resolving model with an eddy permitting model for the representation of convection, it would be interesting to assess how much improvement is brought by the one-kilometer resolution relative to the three-kilometer resolution used by *Herrmann et al*. [2008a]. This should allow the missing processes at the different resolutions to be better quantified.

Winter 2012-2013 was a period in which a number of scientific questions were addressed in a multidisciplinary context. The HyMeX project was aimed at improving the ability of a variety of models (from high resolution to regional climate models) to represent the oceanic convection in realistic conditions of intermittent forcing and the fate of dense water in the Mediterranean basin. The MerMex project was aimed at assessing the budgets of biogenic elements associated with winter convection (replenishment of surface layers with nutrients, oxygen penetration to large depth) and its consequences on the spring bloom.

A more detailed analysis of the simulation in conjunction with CTD data from various platforms (ship, Argo floats, gliders, moorings) deployed during this experiment will help to better understand and quantify the processes occurring at fine scale, such as the Ekman buoyancy flux and the competition between mixing and restratification. An extended simulation will also be necessary to analyze the dispersion of dense water toward the southern basin. The newly-formed dense water should interact with older dense waters formed during the previous winter and still present north of the Balearic Islands. Regarding biogeochemistry, measurements of nutrients and oxygen were made during different cruises. A coupled hydrodynamic biogeochemical model [*Herrmann et al*., 2013; *Auger et al*., 2014] was used to complete these observations and compute the amount of nutrients and organic matter transferred between the bottom and surface layers. Finally, the accuracy of both the space and time representation of dense water formation in the present simulation could be a high-resolution reference for relatively low-resolution regional climate models.

Acknowledgments
This study is a contribution to the MerMex (Marine Ecosystem Response in the Mediterranean Experiment) and HyMeX (Hydrological cycle in the Mediterranean EXperiment) projects of the MISTRALS international program and to the MOOSE (Mediterranean Ocean Observing System on Environment) observation network of the north-western Mediterranean. We acknowledge the support of the project Asics-Med (ANR-12-BS06-0003). Numerical modeling was supported by the PERSEUS project funded by the European Union under FP7, Theme "Oceans of Tomorrow" OCEAN.2011-3, Grant Agreement 287600 and the French ANR COMODO. The authors acknowledge the international ARGO program, the LEFE/GMMC program and the French NAOS project for supporting the deployment of profilers. Argo and CTD data were collected and made freely available by the CORIOLIS project (http://www.coriolis.eu.org) and programs that contribute to it. The outputs of the operational oceanic model were provided by Mercator-Océan. We warmly thank the computer engineers of the Laboratoire d'Aérologie for their technical support. Numerical simulations were performed using HPC resources from CALMIP (grants P09115 and P1325) and the LA cluster. We are grateful to the crews of R/V Suroit and Tethys II and the scientists involved in the different cruises used in this paper. We are very grateful to Vincent Taillandier for the CTD calibration of the MOOSE and DEWEX cruises.

References

Auger, P. A., C. Ulses, C. Estournel, L. Stemmann, S. Somot, and F. Diaz (2014), Interannual control of plankton communities by deep winter mixing and prey/predator interactions in the NW Mediterranean: Results from a 30-year 3D modeling study, *Prog. Oceanogr.*, *124*, 12–27, doi:10.1016/j.pocean.2014.04.004.

Béthoux, J. P., X. Durrieu de Madron, F. Nyffeler, and D. Tailliez (2002), Deep water in the western Mediterranean: Peculiar 1999 and 2000 characteristics, shelf formation hypothesis, variability since 1970 and geochemical inferences, *J. Mar. Syst.*, *33-34*, 117–131, doi:10.1016/S0924-7963(02)00055-6.

Bosse, A. (2015), Circulation générale et couplage physique-biogéochimie à (sous-) mésoéchelle en Méditerranée Nord-Occidentale à partir de données in situ, PhD thesis, Univ. Paris 6 - Pierre et Marie Curie, Paris, France.

Damien, P. (2015), Etude de la circulation océanique en Méditerranée occidentale à l'aide d'un modèle numérique à haute résolution: Influence de la submésoéchelle, PhD thesis, Univ. Paul Sabatier, Toulouse, France. [Available at www.thesesups.ups-tlse.fr/2682.]

Deardorff, J., G. Willis, and D. Lilly (1969), Laboratory investigation of non-steady penetrative convection, *J. Fluid Mech.*, *35*, 7–31.

Durrieu de Madron, X., et al. (2013), Interaction of dense shelf water cascading and open-sea convection in the northwestern Mediterranean during winter 2012, *Geophys. Res. Lett.*, *40*, 1379–1385, doi:10.1002/grl.50331.

Estournel, C., V. Zervakis, P. Marsaleix, A. Papadopoulos, F. Auclair, L. Perivoliotis, and E. Tragou (2005), Dense water formation and cascading in the Gulf of Thermaikos (North Aegean) from observations and modelling, *Cont. Shelf Res.*, *25*, 2366–2386, doi:10.1016/j.csr.2005.08.014.

Gaspar, P., Y. Gregoris, and J. M. Lefevre (1990), A simple eddy kinetic energy model for simulations of the oceanic vertical mixing: Tests at station Papa and long-term upper ocean study site, *J. Geophys. Res.*, *95*(C9), 16,179-16,193.

Grignon, L., D. A. Smeed, H. L. Bryden, and K. Schroeder (2010), Importance of variability of hydrographic preconditioning for deep convection in the Gulf of Lion, NW Mediterranean, *Ocean Sci.*, *6*, 573–586.

Hauser, D., et al. (2003), The FETCH experiment: An overview, *J. Geophys. Res.*, *108*(3), 8053, doi:10.1029/2001JC001202.

Herrmann, M., S. Somot, F. Sevault, C. Estournel, and M. Déqué (2008a), Modeling the deep convection in the northwestern Mediterranean Sea using an eddy-permitting and an eddy-resolving model: Case study of winter 1986-1987, *J. Geophys. Res.*, *113*, C04011, doi:10.1029/2006JC003991.

Herrmann, M., C. Estournel, M. Déqué, P. Marsaleix, F. Sevault, and S. Somot (2008b), Dense water formation in the Gulf of Lions shelf: Impact of atmospheric interannual variability and climate change, *Cont. Shelf Res.*, *28*, 2092–2112, doi:10.1016/j.csr.2008.03.003.

Herrmann, M., F. Sevault, J. Beuvier, and S. Somot (2010), What induced the exceptional 2005 convection event in the Northwestern Mediterranean basin? Answers from a modeling study, *J. Geophys. Res.*, *115*, C12051, doi:10.1029/2010JC006162.

Herrmann, M., S. Somot, S. Calmanti, C. Dubois, and F. Sevault (2011), Representation of spatial and temporal variability of daily wind speed and of intense wind events over the Mediterranean Sea using dynamical downscaling: Impact of the regional climate model configuration, *Nat. Hazards Earth Syst. Sci.*, *11*, 1983_2001, doi:10.5194/nhess-11-1983−2011.

Herrmann, M., F. Diaz, C. Estournel, P. Marsaleix, and C. Ulses (2013), Impact of atmospheric and oceanic interannual variability on the Northwestern Mediterranean Sea pelagic planktonic ecosystem and associated carbon cycle, *J. Geophys. Res.*, *118*, 5792–5813, doi:10.1002/jgrc.20405.

Ivanov, V. V., G. I. Shapiro, J. M. Huthnance, D. L. Aleynik, and P. N. Golovin (2004), Cascades of dense water around the world ocean, *Prog. Oceanogr.*, *60*, 47–98.

Jones, H., and J. Marshall (1997), Restratification after deep convection, *J. Phys. Oceanogr.*, *27*, 2276–2287.

Large, W. G., and S. G. Yeager (2004), Diurnal to decadal global forcing for ocean and sea-ice models: The data sets and flux climatologies, NCAR Tech. Note NCAR/TN-460+STR, NCAR, Boulder, Colo, doi:10.5065/D6KK98Q6.

Lascaratos, A., and K. Nittis (1998), A high-resolution three-dimensional numerical study of intermediate water formation in the Levantine Sea, *J. Geophys. Res.*, *103*, C9, 18,497–18,511 .

Leaman, K. D., and F.A. Schott (1991), Hydrographic Structure of the Convection Regime in the Gulf of Lions: Winter 1987, *J. Phys. Oceanogr.*, *21*, 575–598, doi:10.1175/1520-0485(1991)021<0575:HSOTCR>2.0.CO;2.

Lellouche, J.-M., et al. (2013), Evaluation of global monitoring and forecasting systems at Mercator Océan, *Ocean Sci.*, *9*, 57–81, doi:10.5194/os-9-57-2013.

L'Hévéder, B., L. Li, F. Sevault and S. Somot (2013), Interannual variability of deep convection in the Northwestern Mediterranean simulated with a coupled AORCM, *Clim. Dyn.*, *41*, 937–960, doi:10.1007/s00382-012-1527-5.

López García, M. J., C. Millot, J. Font, and E. García-Ladona (1994), Surface circulation variability in the Balearic basin, *J. Geophys. Res.*, *99*(C2), 3285–3296.

López-Jurado, J. L., C. González-Pola, and P. Vélez-Belchí (2005), Observation of an abrupt disruption of the long-term warming trend at the Balearic Sea, western Mediterranean Sea, in summer, *Geophys. Res. Lett.*, *32*, L24606, doi:10.1029/2005GRL024430.

Manca, B., B, V. Kovačević, M. Gačić, and D. Viezzoli (2002), Dense water formation in the Southern Adriatic Sea and spreading into the Ionian Sea in the period 1997–1999, *J. Mar. Syst.*, *33–34*, 133–154.

Marsaleix P., F. Auclair, J. W. Floor, M. J. Herrmann, C. Estournel, I. Pairaud, and C. Ulses (2008), Energy conservation issues in sigma-coordinate free-surface ocean models, *Ocean Modell.*, *20*, 61–89.

Marsaleix, P., F. Auclair, and C. Estournel (2009), Low-order pressure gradient schemes in sigma coordinate models: The seamount test revisited, *Ocean Modell.*, *30*, 169–177, doi:10.1016/j.ocemod.2009.06.011.

Marsaleix, P., F. Auclair, T. Duhaut, C. Estournel, C. Nguyen, and C. Ulses (2012), Alternatives to the Robert-Asselin filter, *Ocean Modell.*, *41*, 53–66, doi:10.1016/j.ocemod.2011.11.002.

Marshall, J., and F. Schott (1999), Open-ocean convection: Observations, theory, and models, *Rev. Geophys.*, *37*(1), 1–64, doi: 10.1029/98RG02739.

Marsland, S. J., H. Haak, J. H. Jungclaus, M. Latif, and F. Röske (2003), The Max-Planck-Institute global ocean/sea ice model with orthogonal curvilinear coordinates, *Ocean Modell.*, *5*, 91–127.

Mertens, C., and F. Schott (1998), Interannual variability of deep-water formation in the northwestern Mediterranean, *J. Phys. Oceanogr.*, *28*, 1410–1424.

Millot, C. (1987), Circulation in the western Mediterranean Sea, *Oceanol. Acta*, *10*, 143–149.

Nittis, K., A. Lascaratos, and A. Theocharis (2003), Dense water formation in the Aegean Sea: Numerical simulations during the Eastern Mediterranean Transient, *J. Geophys. Res.*, *108*(C9), 8120, doi:10.1029/2002JC001352.

Pettenuzzo, D., W. G. Large, and N. Pinardi (2010), On the corrections of ERA-40 surface flux products consistent with the Mediterranean heat and water budgets and the connection between basin surface total heat flux and NAO, *J. Geophys. Res.*, *115*, C06022, doi:10.1029/2009JC005631.

Puig, P., et al. (2013), Thick bottom nepheloid layers in the western Mediterranean generated by deep dense shelf water cascading, *Prog. Oceanogr.*, *111*, 1–23.
Schott F, M. Visbeck, U. Send, J. Fischer, L. Stramma, and Y. Desaubies (1996), Observations of deep convection in the Gulf of Lion, Northern Mediterranean, during the winter of 1991/1992, *J. Phys. Oceanogr.*, *26*, 505–524.
Schröder, K., G. P. Gasparini, M. Tangherlini, and M. Astraldi (2006), Deep and intermediate water in the western Mediterranean under the influence of the Eastern Mediterranean Transient, *Geophys. Res. Lett.*, *33*, L21607, doi:10.1029/2006GL027121.
Schroeder, K., J. Chiggiato, H. L. Bryden, M. Borghini and S. Ben Ismail (2016), Abrupt climate shift in the Western Mediterranean Sea, *Sci. Rep.*, *6*, 23009; doi:10.1038/srep23009.
Sproson, D. A. J., I. A. Renfrew, and K. J. Heywood (2008), Atmospheric conditions associated with oceanic convection in the south-east Labrador Sea, *Geophys. Res. Lett.*, *35*, L06601, doi:10.1029/2007GL032971.
Taupier-Letage, I., and C. Millot (1988), Surface circulation in the Algerian basin during 1984, *Oceanol. Acta*, *9*, 79–85.
Taylor, J. R., and R. Ferrari (2010), Buoyancy and wind-driven convection at mixed layer density fronts, *J. Phys. Oceanogr.*, *40*, 1222–1242.
Testor, P. (2013), DEWEX-MERMEX 2013 LEG1 cruise, RV Le Suroît, doi:10.17600/13020010.
Testor, P., and J. C. Gascard (2006), Post-convection spreading phase in the Northwestern Mediterranean Sea, *Deep Sea Res., Part I*, *53*, 869–893.
Testor, P., L. Coppola, and L. Mortier (2012), MOOSE-GE 2012 cruise, RV Le Suroît, doi:10.17600/12020030.
Thomas, L. (2005), Destruction of potential vorticity by winds, *J. Phys. Oceanogr.*, *35*, 2457–2466.
Ulses, C., C. Estournel, P. Puig, X. Durrieu de Madron, and P. Marsaleix (2008), Dense water cascading in the northwestern Mediterranean during the cold winter 2005. Quantification of the export through the Gulf of Lion and the Catalan margin, *Geophys. Res. Lett.*, *35*, L07610, doi:10.1029/2008GL033257.
Visbeck, M., J. Marshall, and H. Jones (1996), Dynamics of isolated convective regions in the ocean, *J. Phys. Oceanogr.*, *26*, 1721–1734.